Manufacturing Cost and Reliability-based Shape Optimisation of Plate Structures

Llewellyn Morse[1], Vincenzo Mallardo[1], and M.H. Aliabadi[2]

[1]Department of Architecture, University of Ferrara, Via Quartieri 8, 44121 Ferrara, Italy

[2]Department of Aeronautics, Imperial College London, South Kensington Campus, City and Guilds Building, Exhibition Road, SW7 2AZ, London, UK

December 28, 2021

Abstract

A novel methodology is presented for the manufacturing cost and reliability-based optimisation of plate structures with the Boundary Element Method (BEM), with the aim of improving the accuracy, robustness, and efficiency of the optimisation of aircraft structures. The BEM plate formulations with respect to plate thickness are derived for the first time, and used as part of an Implicit Differentiation Method (IDM), enabling the full shape optimisation of plate structures with the BEM. These implicit derivatives are validated against derivatives obtained from the Finite Difference Method (FDM) and from an analytical solution. Results indicate that the IDM is more robust than the FDM and in excellent agreement with the analytical solution, and more accurate than the FDM for most of the step-sizes investigated. To demonstrate the full shape optimisation of plates with the newly developed IDM, a numerical example involving Reliability-Based Design Optimisation (RBDO) and manufacturing cost optimisation is presented for a plate structure. Results show that the newly developed IDM is more efficient than the FDM when performing this optimisation.

1 Introduction

Structural mass is a very important consideration for aeronautical engineers, as small increases in the mass of an aircraft can lead to significant increases in fuel consumption and carbon emissions. Alongside mass, manufacturing costs are also a significant consideration for aeronautical engineers. Reductions in manufacturing costs can enable aircraft manufacturers to divert more resources towards improving safety and reducing the environmental impact of their aircraft. Reductions in costs could also be passed down to consumers via reduced ticket prices. Reliability-Based Design Optimisation (RBDO) can often provide designs for structures that are optimised in terms of mass and reliability, but not necessarily in terms of manufacturing costs, especially for complex structures. This work aims to develop a methodology that couples the RBDO of aircraft structures with a manufacturing cost estimation approach.

Optimising a structure for manufacturing cost and reliability involves shape optimisation - optimising the shape of a structure to minimise manufacturing cost and to maximise reliability. The Boundary

This article has been accepted for publication and undergone full peer review but has not been through the copyediting, typesetting, pagination and proofreading process which may lead to differences between this version and the Version of Record. Please cite this article as doi: 10.1002/nme.6931

Element Method (BEM) can be a very effective tool for shape optimisation. The BEM only discretises the outer boundary of a structure, allowing the outer geometry to be varied without requiring the entire structure to be resmeshed, saving both time and computational resources. An added benefit of this feature is that it allows the sensitivities of the responses of a BEM model, with respect to changes in the outer geometry, to be calculated in a very straightforward and computationally efficient manner, making the BEM a very effective tool for the shape optimisation of engineering structures.

Previous work on the topic of shape optimisation with the BEM by the research community has mostly considered 2D structures [1–11], and to a lesser-degree 3D structures [12–18]. Very few previous works by the research community on the topic of shape optimisation with the BEM have considered plate or shell structures. Where possible, modelling a structure as a plate or shell structure can have significant benefits over modelling the structure in 2D or 3D. This is because many real-life engineering structures cannot be accurately modelled as 2D structures, and depending on the engineering structure being modelled, it can often be more efficient to model a structure as a plate or a shell structure, rather than as a 3D structure, without a noticable loss in modelling accuracy. An example of this could be a curved stiffened panel from an aircraft fuselage, or a wingbox from an aircraft's wing. To the authors' knowledge, there is only one previous work by the research community on the topic of shape optimisation with the BEM with plate or shell structures; Babouskos et al. [19] optimised the thickness distribution in a thin plate to regulate the dynamic response of the plate. The thickness distribution of the plate was approximated via a surrogate model, and the optimal thickness distribution in the plate was calculated using derivatives of this surrogate model. The derivatives of the BEM formulations for plates were not calculated, and the remaining geometry of the plate was not optimised. This current work aims to develop an Implicit Differentiation Method (IDM), which uses the implicit/direct derivatives of the BEM formulations for plates, to enable the full shape optimisation of plate structures with the BEM, involving all of a plate's geometry. By using the implicit/direct derivatives of the BEM formulations, shape optimisation can be conducted in a much more accurate and efficient manner than with other methods.

The first steps towards developing an IDM for plate or shell structures with the BEM were conducted by Morse et al. in [20], in which the exact/implicit derivatives of the BEM plate formulations with respect to geometrical variables were derived for the first time. These exact derivatives were only applicable to geometrical variables that influence the nodal coordinates of the BEM plate mesh, such as plate length or width, and so they were not applicable to geometrical variables that do not influence nodal coordinates, such as plate thickness. Therefore, the full shape optimisation of plate structures, involving all geometrical variables, was not possible. This current work aims to build upon the work presented in [20] and enable the full shape optimisation of plate structures, involving all geometrical variables. This is achieved by deriving the exact/implicit derivatives of the BEM plate formulations with respect to plate thickness for the first time.

Previous work by the research community involving exact \implicit derivatives of BEM formulations have focused on 2D structures [1,3,21–28], with some work conducted on 3D structures [13,29], and one work so far on plate structures [20]. One notable example is Huang et al. in which the implicit derivatives for the 2D Dual Boundary Element Method (DBEM), a version of BEM effective at modelling cracks, were developed for the first time and used to estimate the reliability of 2D structures using the First-Order Reliability Method (FORM). Another notable example is Brancati et al. [13], in which the implicit derivatives of 3D boundary element formulations were used to optimise noise levels in an aircraft cabin.

In summary, the main novelty of this work is that the exact/implicit derivatives of the BEM plate formulations with respect to plate thickness have been derived for the first time, enabling the full

shape optimisation of plate structures with the BEM. These implicit derivatives will be validated against derivatives obtained from the Finite Difference Method (FDM) and from an analytical solution. To demonstrate the full shape optimisation of plates with the BEM, a numerical example involving Reliability-Based Design Optimisation (RBDO) and manufacturing cost optimisation is presented.

The methodology behind manufacturing cost estimation is presented in section 2, followed by the methodology used for RBDO in section 3. The implicit derivatives of the BEM plate formulations with respect to plate thickness are presented in section 4, alongside the validation of these implicit derivatives. The numerical example involving RBDO and manufacturing cost estimation is shown in section 5. The implicit derivatives of the BEM plate fundamental solutions with respect to plate thickness are presented in detail in the Appendix.

2 Parametric Approach to Manufacturing Cost Estimation

The parametric cost estimation methodology used in this work is based on the parametric cost estimation methodology described in detail in Appendix C of the NASA Cost Estimating Handbook [30].

A parametric model can be created to estimate the manufacturing cost of a structural component. The parametric model used in this work is a linear regression of the following form:

$$Cost = \beta_0 + \beta_1 x_1 + \beta_2 x_2 \ldots + \beta_k x_k \tag{1}$$

where *Cost* is the manufacturing cost of a structural component, and $[x_1, x_2, \ldots x_k]$ are independent variables that influence the manufacturing cost, also known as *cost drivers*. $[\beta_1, \beta_2, \ldots \beta_k]$ are regression coefficients. The cost drivers could be the dimensions of a structural component, such as its length and width. The creation of this parametric model required the use of a historical database containing the details of similar structural components, and could be created by collecting the details of structural components from a range of similar aircraft models. In this work, this database is an artificial database created by the authors.

To minimise the effects of multicollinearity, a stepwise regression approach is taken when creating the regression model seen in equation (1). The most important cost drivers are identified based on their Pearson correlations coefficient with respect to the manufacturing cost. The most important cost driver is used as the sole independent variable of the first iteration of stepwise regression procedure. In the following iterations, the next most important cost drivers are added to the model. If the addition of a driver noticeably improved the model, it is kept in the model, otherwise it is removed. This is repeated until all of the important cost drivers have been tried in the model. Therefore, the resulting regression model will include only the very most important cost drivers, mitigating the effects of multicollinearity and providing an accurate parametric model for estimating the manufacturing cost of a structure.

3 Reliability-based Design Optimisation (RBDO)

In the field of reliability analysis, the boundary between succeeding or failing to meet a certain set of criteria can be represented mathematically by a limit state function (LSF) $g(\mathbf{Z})$. For example, if we are looking at the probability of a structure failing due to load, the LSF will be:

$$g(\mathbf{Z}) = R - S(\mathbf{Q}) \tag{2}$$

where $\mathbf{Z}$ is a vector of random variables ($\mathbf{Z} \in \mathbb{R}^{n_r}$ where n_r is the number of random variables), and $\mathbf{Q}$ is a subset of $\mathbf{Z}$ if R is a random variable, where R is the resistance of the structure to some load S. If $S(\mathbf{Q}) > R$ then $g(\mathbf{Z}) < 0$ and the structure is considered to have failed, while if $S(\mathbf{Q}) \leq R$ then $g(\mathbf{Z}) \geq 0$ and the structure is considered safe.

The probability that the set of criteria has failed to be met is termed the *probability of failure* P_F, while the probability that the set of criteria has been successfully met is termed *reliability* P_R. In the example outlined above, these probabilities would correspond to the probabilities of the structure failing or being safe under the load S respectively. Reliability can be determined by evaluating the following integral:

$$P_R = 1 - P_F = P\{g(\mathbf{Z}) > 0\} = \int\limits_{g(\mathbf{Z})>0} f_{\mathbf{Z}}(\mathbf{Z}) d\mathbf{Z} \tag{3}$$

where $f_{\mathbf{Z}}(\mathbf{Z})$ is the joint PDF of $\mathbf{Z}$. P_R and P_F are obtained by integrating over the failure region ($g(\mathbf{Z}) < 0$) and the safe region ($g(\mathbf{Z}) \geq 0$) respectively. All of the design variables are assumed to be mutually independent. The integral seen in equation (3) can be difficult to evaluate if there are many variables in $\mathbf{X}$ or if the boundary $g(\mathbf{Z}) = 0$ is non-linear. Therefore, several methods have been developed to evaluate the integral in equation (3). The most widely known are Monte Carlo Simulations (MCS), the First-Order Reliability Method (FORM), and the Second-Order Reliability Method (SORM). This work will focus on the FORM due to its efficiency.

The reliability P_R shown in (3) can be represented in terms of a reliability index β as:

$$P_R = 1 - P_F = 1 - \Phi(-\beta) = \Phi(\beta) \tag{4}$$

where Φ denotes the CDF of the standard normal distribution. A large value for the reliability P_R corresponds to a large value for the reliability index β. β can be found by rearranging the above equation to yield:

$$\beta = \Phi^{-1}(P_R) = \Phi^{-1}(1 - P_F) \tag{5}$$

where Φ^{-1} is the inverse of the CDF of the standard normal distribution.

Reliability-based Design Optimisation (RBDO) involves optimising the design of a structure such that the reliability of the structure achieves a certain level of reliability. There are two main approaches to RBDO, the Reliability Index Approach (RIA) and the Performance Measure Approach (PMA).

3.1 Reliability Index Approach (RIA) to RBDO

In the RIA, the optimisation problem is:

$$\begin{aligned} &\text{Minimise} && Cost(\mathbf{d}) \\ &\text{Subject to} && \beta_{FORM} \geq \beta_{target} \\ & && \mathbf{d}^L \leq \mathbf{d} \leq \mathbf{d}^U, \quad \mathbf{d} \in \mathbb{R}^{n_d} \end{aligned} \tag{6}$$

where $\mathbf{d}$ is a vector of n_d design variables ($\mathbf{d} \subseteq \mu(\mathbf{Q})$ and $n_d \leq n_r$), β_{FORM} is the reliability index from FORM, and β_{target} is the target reliability index. $\mathbf{d}^L$ and $\mathbf{d}^U$ are vectors containing the lower and upper bounds respectively of the design variables.

For a given vector of random variables $\mathbf{Z}$, the RIA calculates the reliability index β via FORM for each iteration of the optimisation procedure.

3.2 Performance Measure Approach (PMA) to RBDO

In the PMA, the optimisation problem is:

$$\begin{aligned} &\text{Minimise} && Cost(\mathbf{d}) \\ &\text{Subject to} && g(\mathbf{Z}^*) \leq 0 \\ & && \mathbf{d}^L \leq \mathbf{d} \leq \mathbf{d}^U, \quad \mathbf{d} \in \mathbb{R}^{n_d} \end{aligned} \tag{7}$$

where $g(\mathbf{Z}^*)$ is the value of the limit state function evaluated at the Most Probable Point (MPP) found from the PMA. The PMA algorithm used in this work is the Hybrid Mean Value (HMV) algorithm [31], due to its enhanced efficiency and stability.

The PMA can be thought of as the inverse of the RIA. For a given vector of random variables $\mathbf{Z}$, the PMA calculates the MPP point $\mathbf{Z}^*$ for which $\beta_{FORM} = \beta_{target}$. This MPP $\mathbf{Z}^*$ is then used by the next iteration of the optimization procedure.

The PMA requires the derivatives of the constaints, i.e. the limit state function g in equation (7), to be calculated. In this work, g will be a function of boundary stresses or internal displacements. Therefore, the derivatives of the boundary stresses and internal displacements need to be derived. Since the Boundary Element Method (BEM) is used in this work to calculate boundary stresses or internal displacements, the derivatives of the BEM formulations for plate structures will need to be derived. These derivatives have been derived for the first time and are presented in the next section.

4 RBDO Constraint Derivatives

To improve the computational efficiency of conducting RBDO for plate structures using the PMA approach, the exact derivatives of the response of a BEM plate model were derived for the first time.

In this work, Latin letter indexes (e.g. i, j, k) can take values from 1 to 3, while Greek letter indexes (e.g. α, β, ρ, γ) can take values of either 1 or 2.

4.1 BEM Formulations for Plates

In this section, the BEM formulations for plates are presented.

Consider the plate of thickness h shown in Figure 1. The $x_1 - x_2$ plane is the middle surface $x_3 = 0$, or membrane, of the plate where $-h/2 \leq x_3 \leq +h/2$. x_3 can be described in terms of a non-dimensional variable $\bar{x}_3$, such that $x_3 = \bar{x}_3 h$, where $-1/2 \leq \bar{x}_3 \leq +1/2$.

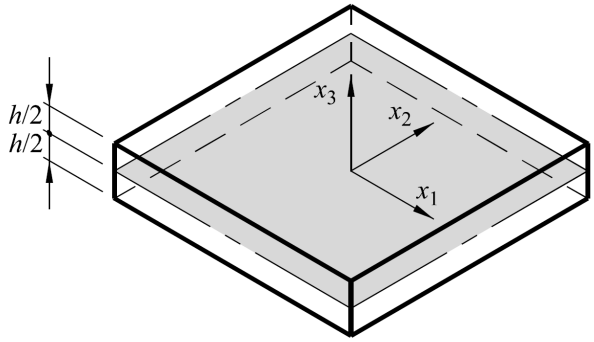

Figure 1: Plate geometry [32].

The displacements of the plate are u_α, where u_1 and u_2 are the displacements in the directions x_1 and x_2 respectively. The rotations of the plate are w_α, where w_1 and w_2 are the rotations of the plate in the directions x_1 and x_2 respectively. The displacement of the plate in the direction x_3 is w_3. The tractions are denoted as t_α and p_i. t_α are tractions due to membrane stress resultants $N_{\alpha\beta}$. p_α are tractions due to bending stress resultants $M_{\alpha\beta}$. p_3 denotes traction due to shear stress resultants Q_α. A diagram explaining the sign convention of these displacements, rotations, and tractions for plate bending can be seen in Figure 2.

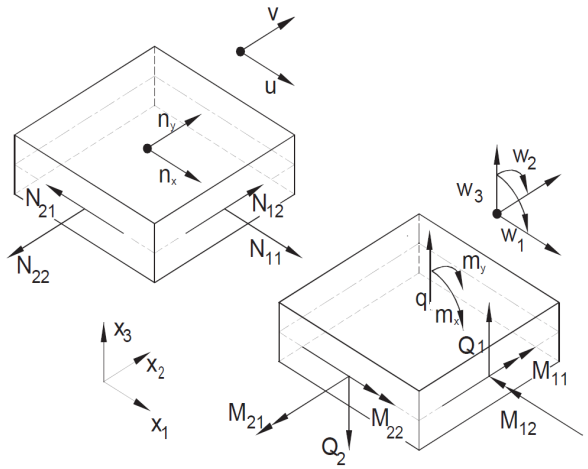

Figure 2: Sign convection for displacement, rotations, tractions, and moments for shear deformable plates [33].

4.1.1 Boundary Integral Equations

From [34], the discretised BEM boundary integral equations for plate bending are shown below.

The discretised BEM boundary integral equation for the plate membrane is:

$$C^m_{\alpha\beta}(\mathbf{x}^{n_c})u_\beta(\mathbf{x}^{n_c}) + \sum_{n_e=1}^{N_e}\sum_{\gamma=1}^{M} P^{m,n_e\gamma}_{\alpha\beta}(\mathbf{x}^{n_c})u^{n_e\gamma}_\beta = \sum_{n_e=1}^{N_e}\sum_{\gamma=1}^{M} Q^{m,n_e\gamma}_{\alpha\beta}(\mathbf{x}^{n_c})t^{n_e\gamma}_\beta \tag{8}$$

where:

$$P^{m,n_e\gamma}_{\alpha\beta}(\mathbf{x}^{n_c}) = \fint_{-1}^{+1} T^m_{\alpha\beta}(\mathbf{x}^{n_c},\mathbf{x}(\eta))S^{n_e\gamma}(\eta)J^{n_e}(\eta)d\eta \tag{9}$$

$$Q^{m,n_e\gamma}_{\alpha\beta}(\mathbf{x}^{n_c}) = \int_{-1}^{+1} U^m_{\alpha\beta}(\mathbf{x}^{n_c},\mathbf{x}(\eta))S^{n_e\gamma}(\eta)J^{n_e}(\eta)d\eta \tag{10}$$

where $\mathbf{x}^{n_c}$, $n_c = 1,2,\ldots,N_c$ (where $N_c = N_n$) is the collocation node, N_n is the number of nodes, N_e is the number of elements, and M is the number of nodes per element. $M = 3$ in the case of quadratic elements. Superscript m indicates that an equation is for the plate membrane. $S^{n_e\gamma}$ is the shape function of node γ of element n_e, and J^{n_e} is the Jacobian of element n_e. $P^{m,n_e\gamma}_{\alpha\beta}$ and $Q^{m,n_e\gamma}_{\alpha\beta}$ are fundamental solutions evaluated at node γ of element n_e. $u^{n_e\gamma}_\beta$ are in-plane displacements at node γ of element n_e, and $t^{n_e\gamma}_\beta$ are tractions due to membrane stress resultants $N_{\alpha\beta}$ at node γ of element n_e.

The discretised form of the displacement boundary integral equation for bending is:

$$C^b_{ij}(\mathbf{x}^{n_c})w_j(\mathbf{x}^{n_c}) + \sum_{n_e=1}^{N_e}\sum_{\gamma=1}^{M} P^{b,n_e\gamma}_{ij}(\mathbf{x}^{n_c})w^{n_e\gamma}_j = \sum_{n_e=1}^{N_e}\sum_{\gamma=1}^{M} Q^{b,n_e\gamma}_{ij}(\mathbf{x}^{n_c})p^{n_e\gamma}_j + q_3\sum_{n_e=1}^{N_e} O^{b,n_e}_i(\mathbf{x}^{n_c}) \tag{11}$$

where:

$$P^{b,n_e\gamma}_{ij}(\mathbf{x}^{n_c}) = \fint_{-1}^{+1} T^b_{ij}(\mathbf{x}^{n_c},\mathbf{x}(\eta))S^{n_e\gamma}(\eta)J^{n_e}(\eta)d\eta \tag{12}$$

$$Q^{b,n_e\gamma}_{ij}(\mathbf{x}^{n_c}) = \int_{-1}^{+1} U^b_{ij}(\mathbf{x}^{n_c},\mathbf{x}(\eta))S^{n_e\gamma}(\eta)J^{n_e}(\eta)d\eta \tag{13}$$

$$O^{b,n_e}_i(\mathbf{x}^{n_c}) = \int_{-1}^{+1} B^b_i(\mathbf{x}^{n_c},\mathbf{x}(\eta))J^{n_e}(\eta)d\eta \tag{14}$$

where:

$$B^b_i(\mathbf{x}^{n_c},\mathbf{x}(\eta)) = V^b_{i,\alpha}(\mathbf{x}^{n_c},\mathbf{x}(\eta))n_\alpha(\mathbf{x}(\eta)) - \frac{\nu}{(1-\nu)\lambda^2}U^b_{i\alpha}(\mathbf{x}^{n_c},\mathbf{x}(\eta))n_\alpha(\mathbf{x}(\eta)) \tag{15}$$

where superscript b indicates that an equation is for plate bending. $P^{b,n_e\gamma}_{\alpha\beta}$, $Q^{b,n_e\gamma}_{\alpha\beta}$, and O^{b,n_e}_i are fundamental solutions evaluated at node γ of element n_e. $w^{n_e\gamma}_j$ are the rotations and vertical displacement of

the plate (w_1 and w_2 are rotations, and w_3 is vertical displacement) at at node γ of element n_e. $p_\alpha^{n_e\gamma}$ are tractions due to bending stress resultants $M_{\alpha\beta}$, and $p_3^{n_e\gamma}$ denotes traction due to shear stress resultants Q_α, at at node γ of element n_e. q_3 is constant uniform loading over the entire top surface of the plate. ν is the Poisson's ratio, and $\lambda = \sqrt{10}/h$ is the shear factor, where h is the thickness of the plate.

In the above equations, T_{ij}^b, U_{ij}^b, and $V_{i,\alpha}^b$ are the fundamental solutions for plate bending, while $T_{\alpha\beta}$ and $U_{\alpha\beta}$ are the fundamental solutions for the membrane. Expressions for these fundamental solutions can be found in [32]. The integral symbol $\oint$ represents Cauchy principal value integrals. w_1 and w_2 denote rotations in the directions x_1 and x_2 respectively, and w_3 denotes displacement in the direction x_3. u_1 and u_2 are the displacements in the directions x_1 and x_2 respectively. p_k are the bending and shear tractions with $p_\alpha = M_{\alpha\beta}n_\beta$ and $p_3 = Q_\alpha n_\alpha$. t_1 and t_2 are membrane tractions in the directions x_1 and x_2 respectively where $t_\alpha = N_{\alpha\beta}n_\beta$. The integrations are carried out over the boundary S of the structure's domain. The terms $C_{\alpha\beta}^m$ and C_{ij}^b are free terms and their values can be directly evaluated from a consideration of rigid body motion [32].

Since the fundamental solutions shown in the integral equations (9)-(10), and (49)-(52) are of the order of $\ln(1/r)$ or $1/r$, (where r is the distance between the collocation node and the field point) mathematical singularities can occur when the collocation node lies within the same element as the field point. Weakly singular integrals are defined as integrals with singularities of the order $\ln(1/r)$ or $1/r$ such as those seen in equations (49)-(52) and (9)-(10). In this case, the transformation of variable technique proposed by Telles [35] is used. For equations (49) and (9), rigid body motion is also applied. For each of the integral equations seen above, when the collocation node is near to the field point, but is not in the same element as the field point, the integral shows near-singular behaviour. In this case, the element subdivision technique is used. Details on these methods can be found in [32].

The system of equations used in the BEM is of the form $\mathbf{Hu} = \mathbf{Gt}$. Where $\mathbf{H}$ is a $(5N_n \times 5N_n)$ matrix, and $\mathbf{G}$ is a $(5N_n \times 5N_eM)$ matrix. $\mathbf{u}$ is a $(5N_n \times 1)$ vector of known and unknown displacements, and $\mathbf{t}$ is a $(5N_eM \times 1)$ vector of known and unknown tractions. The final system of equations can be written as:

$$\mathbf{AX} = \mathbf{F} \tag{16}$$

where $\mathbf{A}$ is a $(5N_n \times 5N_n)$ usually unsymmetric and dense coefficient matrix composed of parts of $\mathbf{H}$ and $\mathbf{G}$, $\mathbf{X}$ is a $(5N_n \times 1)$ vector containing all of the unknown boundary displacements and tractions, and $\mathbf{F}$ is a $(5N_n \times 1)$ vector containing parts of $\mathbf{G}$ multiplied by known tractions and parts of $\mathbf{H}$ multiplied by known displacements. This system of equations, after applying the boundary conditions, can be solved using LU decomposition.

An example of a BEM mesh for a simple plate structure can be seen in Figure 3.

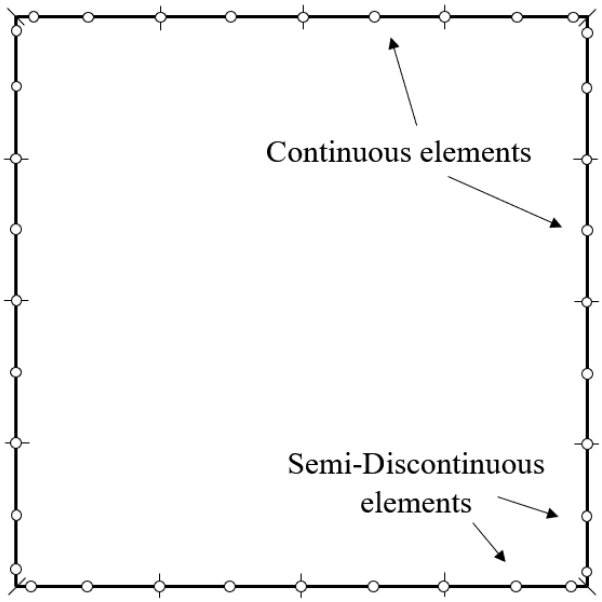

Figure 3: An example of mesh design for a square plate. Quadratic elements consisting of three nodes are used. White circles indicate the location of nodes.

As seen in Figure 3, the boundary of a structure is discretised using continuous quadratic elements except at the corners - where due to the non-uniqueness of the normals, semi-discontinuous quadratic elements are used.

4.1.2 Displacements and Rotations at Internal Points

The displacements and rotations at internal points can be evaluated using the solution $\mathbf{X}$ to the system of equations. The in-plane displacements at some internal point $\mathbf{X}^{n_i}$, $n_i = 1,2,\ldots,N_i$ (where N_i is the number of internal points) are:

$$u_\beta(\mathbf{X}^{n_i}) + \sum_{n_e=1}^{N_e}\sum_{\gamma=1}^{M} P_{\alpha\beta}^{m,n_e\gamma}(\mathbf{X}^{n_i})u_\beta^{n_e\gamma} = \sum_{n_e=1}^{N_e}\sum_{\gamma=1}^{M} Q_{\alpha\beta}^{m,n_e\gamma}(\mathbf{X}^{n_i})t_\beta^{n_e\gamma} \tag{17}$$

where:

$$P_{\alpha\beta}^{m,n_e\gamma}(\mathbf{X}^{n_i}) = \int_{-1}^{+1} T_{\alpha\beta,\rho}^{m}(\mathbf{X}^{n_i},\mathbf{x}(\eta))S^{n_e\gamma}(\eta)J^{n_e}(\eta)d\eta \tag{18}$$

$$Q_{\alpha\beta}^{m,n_e\gamma}(\mathbf{X}^{n_i}) = \int_{-1}^{+1} U_{\alpha\beta,\rho}^{m}(\mathbf{X}^{n_i},\mathbf{x}(\eta))S^{n_e\gamma}(\eta)J^{n_e}(\eta)d\eta \tag{19}$$

The rotations w_1 and w_2, and vertical displacement (out-of-plane displacement) w_3, are:

$$w_j(\mathbf{X}^{n_i}) + \sum_{n_e=1}^{N_e}\sum_{\gamma=1}^{M} P_{ij}^{b,n_e\gamma}(\mathbf{X}^{n_i})w_j^{n_e\gamma} = \sum_{n_e=1}^{N_e}\sum_{\gamma=1}^{M} Q_{ij}^{b,n_e\gamma}(\mathbf{X}^{n_i})p_j^{n_e\gamma} + q_3\sum_{n_e=1}^{N_e} O_i^{b,n_e}(\mathbf{X}^{n_i}) \tag{20}$$

where:

$$P_{ij}^{b,n_e\gamma}(\mathbf{X}^{n_i}) = \int_{-1}^{+1} T_{ij}^{b}(\mathbf{X}^{n_i},\mathbf{x}(\eta))S^{n_e\gamma}(\eta)J^{n_e}(\eta)d\eta \tag{21}$$

$$Q_{ij}^{b,n_e\gamma}(\mathbf{X}^{n_i}) = \int_{-1}^{+1} U_{ij}^{b}(\mathbf{X}^{n_i},\mathbf{x}(\eta))S^{n_e\gamma}(\eta)J^{n_e}(\eta)d\eta \tag{22}$$

$$O_{i}^{b,n_e}(\mathbf{X}^{n_i}) = \int_{-1}^{+1} B_{i}^{b}(\mathbf{X}^{n_i},\mathbf{x}(\eta))J^{n_e}(\eta)d\eta \tag{23}$$

and:

$$\begin{aligned} B_i^b(\mathbf{X}^{n_i},\mathbf{x}(\eta)) = {} & V_{i,\alpha}^b(\mathbf{X}^{n_i},\mathbf{x}(\eta))n_\alpha(\mathbf{x}(\eta)) \\ & - \frac{\nu}{(1-\nu)\lambda^2}U_{i\alpha}^b(\mathbf{X}^{n_i},\mathbf{x}(\eta))n_\alpha(\mathbf{x}(\eta)) \end{aligned} \tag{24}$$

4.1.3 Boundary Stress Resultants

In shear deformable plate theory, the normal stress components $\sigma_{\alpha\beta}$ are assumed to vary linearly through the thickness of the plate. Therefore:

$$\sigma_{\alpha\beta} = \frac{1}{h}N_{\alpha\beta} + \frac{12x_3}{h^3}M_{\alpha\beta} \tag{25}$$

where $N_{\alpha\beta}$ are the membrane stress resultants, $M_{\alpha\beta}$ are the bending stress resultants, and $-h/2 \leq x_3 \leq +h/2$ (see Figure 1).

In this work, an indirect approach is used to evaluate boundary stresses. The boundary stresses are evaluated from boundary tractions and tangential strains. More detail on this method can be found in [32]. A brief description of this method is outlined below.

A local coordinate system can be defined on a boundary element n_e such that $\hat{e}_{1\beta}^{n_e}(\eta)$ (where $\hat{e}_{1\beta}^{n_e}(\eta) = n_\beta^{n_e}(\eta)$, $\beta = 1,2$) is a unit vector in the normal direction to the boundary element, and $\hat{e}_{2\beta}^{n_e}(\eta)$ is a unit vector in the tangential direction to the boundary element. Therefore, the local coordinates of node γ of element n_e are:

$$\hat{x}_\alpha^{n_e\gamma} = \hat{e}_{1\alpha}^{n_e\gamma}x_1^{n_e\gamma} + \hat{e}_{2\alpha}^{n_e\gamma}x_2^{n_e\gamma} \tag{26}$$

where $\hat{e}_{\alpha\beta}^{n_e\gamma} = \hat{e}_{\alpha\beta}^{n_e}(\eta_\gamma)$, and $x_\beta^{n_e\gamma}$ are the global coordinates of node γ of element n_e. Therefore, the rotation matrix $\hat{e}_{\alpha\beta}$ for node γ of element n_e can be written as:

$$\hat{e}_{\alpha\beta}^{n_e\gamma} = \begin{bmatrix} \hat{e}_{11}^{n_e\gamma} & \hat{e}_{12}^{n_e\gamma} \\ \hat{e}_{21}^{n_e\gamma} & \hat{e}_{22}^{n_e\gamma} \end{bmatrix} = \begin{bmatrix} n_1^{n_e\gamma} & n_2^{n_e\gamma} \\ -n_2^{n_e\gamma} & n_1^{n_e\gamma} \end{bmatrix} \tag{27}$$

This local coordinate system can be seen in Figure 4.

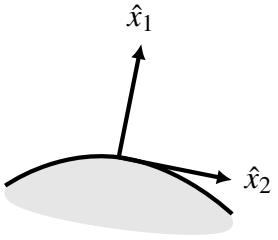

Figure 4: Local coordinate system for boundary stress calculation.

If $\hat{u}_\beta^{n_e\gamma}$, $\hat{\varepsilon}_{\alpha\beta}^{n_e\gamma}$, $\hat{N}_{\alpha\beta}^{n_e\gamma}$, and $\hat{t}_\beta^{n_e\gamma}$ are the displacements, strains, stresses, and tractions for node γ of element n_e in local coordinates $\hat{x}_\beta$ then the normal component of the local stress:

$$\hat{N}_{1\alpha}^{n_e\gamma} = \hat{t}_\alpha^{n_e\gamma} \tag{28}$$

The tangential component of the local stress is:

$$\hat{N}_{22}^{n_e\gamma} = \frac{1}{1-\nu}\left[\frac{Eh}{1+\nu}\hat{\varepsilon}_{22}^{n_e\gamma} + \nu\hat{t}_1^{n_e\gamma}\right] \tag{29}$$

where $\hat{\varepsilon}_{22}^{n_e\gamma} = \partial\hat{u}_2^{n_e\gamma}/\partial\hat{x}_2$, and is given by:

$$\hat{\varepsilon}_{22}^{n_e\gamma} = \frac{\hat{e}_{2\alpha}^{n_e\gamma}}{J^{n_e}(\eta_\gamma)}\sum_{\rho=1}^{M}\left(u_\alpha^{n_e\rho}\left(\frac{dN^{n_e\rho}(\eta)}{d\eta}\right)_{\eta=\eta_\gamma}\right) \tag{30}$$

The local boundary stresses can now be calculated using equations (28) and (29). The global stresses $N_{\alpha\beta}^{n_e\gamma}$ can be calculated from the local stresses $\hat{N}_{\alpha\beta}^{n_e\gamma}$ via:

$$N_{\alpha\beta}^{n_e\gamma} = \hat{e}_{\rho\alpha}\hat{e}_{\phi\beta}\hat{N}_{\rho\phi}^{n_e\gamma} \tag{31}$$

Using the relationships in equation (27), the global membrane stress resultants can be obtained:

$$\begin{aligned}
N_{11}^{n_e\gamma} &= (n_1^{n_e\gamma})^2\hat{N}_{11}^{n_e\gamma} + (n_2^{n_e\gamma})^2\hat{N}_{22}^{n_e\gamma} - 2n_1^{n_e\gamma}n_2^{n_e\gamma}\hat{N}_{12}^{n_e\gamma} \\
N_{12}^{n_e\gamma} &= n_1^{n_e\gamma}n_2^{n_e\gamma}(\hat{N}_{11}^{n_e\gamma} - \hat{N}_{22}^{n_e\gamma}) \\
&\quad + \left[(n_1^{n_e\gamma})^2 - (n_2^{n_e\gamma})^2\right]\hat{N}_{12}^{n_e\gamma} \\
N_{22}^{n_e\gamma} &= (n_2^{n_e\gamma})^2\hat{N}_{11}^{n_e\gamma} + (n_1^{n_e\gamma})^2\hat{N}_{22}^{n_e\gamma} + 2n_1^{n_e\gamma}n_2^{n_e\gamma}\hat{N}_{12}^{n_e\gamma}
\end{aligned} \tag{32}$$

The out-of-plane stress resultants can be calculated in a similar manner as the in-plane stress resultants.

The normal components of the tractions at node γ of element n_e are:

$$\hat{p}_1^{n_e\gamma} = n_1^{n_e\gamma}p_1^{n_e\gamma} + n_2^{n_e\gamma}p_2^{n_e\gamma} \tag{33}$$

The tangential component of tractions are:

$$\hat{p}_2^{n_e\gamma} = -n_2^{n_e\gamma}p_1^{n_e\gamma} + n_1^{n_e\gamma}p_2^{n_e\gamma} \tag{34}$$

The tangential component of the rotations are:

$$\hat{w}_2^{n_e\gamma} = -n_2^{n_e\gamma}w_1^{n_e\gamma} + n_1^{n_e\gamma}w_2^{n_e\gamma} \tag{35}$$

The local tangential strain is:

$$\hat{\chi}_{22}^{n_e\gamma} = \frac{\hat{e}_{2\alpha}^{n_e\gamma}}{J^{n_e}(\eta_\gamma)}\sum_{\rho=1}^{M}\left(w_\alpha^{n_e\rho}\left(\frac{dN^{n_e\rho}(\eta)}{d\eta}\right)_{\eta=\eta_\gamma}\right) \tag{36}$$

The local moments and shear stresses are:

$$\hat{M}_{11}^{n_e\gamma} = \hat{p}_1^{n_e\gamma} \tag{37}$$

$$\hat{M}_{12}^{n_e\gamma} = \hat{p}_2^{n_e\gamma} \tag{38}$$

$$\hat{M}_{22}^{n_e\gamma} = \nu \hat{M}_{11}^{n_e\gamma} + D(1-\nu^2)\hat{\chi}_{22}^{n_e\gamma} + \frac{q_3\nu}{\lambda^2} \tag{39}$$

$$\hat{S}_{11}^{n_e\gamma} = p_3^{n_e\gamma} \tag{40}$$

$$\begin{aligned}\hat{S}_{22}^{n_e\gamma} =& \frac{D(1-\nu)\lambda^2}{2}\left[\hat{w}_2^{n_e\gamma}\right. \\ &\left. + \frac{1}{J^{n_e}(\eta_\gamma)}\sum_{\rho=1}^{M}\left(w_3^{n_e\rho}\left(\frac{dN^{n_e\rho}(\eta)}{d\eta}\right)_{\eta=\eta_\gamma}\right)\right]\end{aligned} \tag{41}$$

The global moment stress resultants for node γ of element n_e are:

$$\begin{aligned}M_{11}^{n_e\gamma} &= (n_1^{n_e\gamma})^2\hat{M}_{11}^{n_e\gamma} + (n_2^{n_e\gamma})^2\hat{M}_{22}^{n_e\gamma} - 2n_1^{n_e\gamma}n_2^{n_e\gamma}\hat{M}_{12}^{n_e\gamma} \\ M_{12}^{n_e\gamma} &= n_1^{n_e\gamma}n_2^{n_e\gamma}(\hat{M}_{11}^{n_e\gamma} - \hat{M}_{22}^{n_e\gamma}) \\ &\quad + \left[(n_1^{n_e\gamma})^2 - (n_2^{n_e\gamma})^2\right]\hat{M}_{12}^{n_e\gamma} \\ M_{22}^{n_e\gamma} &= (n_2^{n_e\gamma})^2\hat{M}_{11}^{n_e\gamma} + (n_1^{n_e\gamma})^2\hat{M}_{22}^{n_e\gamma} + 2n_1^{n_e\gamma}n_2^{n_e\gamma}\hat{M}_{12}^{n_e\gamma}\end{aligned} \tag{42}$$

The global shear stress resultants for node γ of element n_e are:

$$S_1^{n_e\gamma} = n_1^{n_e\gamma}\hat{S}_{11}^{n_e\gamma} - n_2^{n_e\gamma}\hat{S}_{22}^{n_e\gamma} \tag{43}$$

$$S_2^{n_e\gamma} = n_2^{n_e\gamma}\hat{S}_{11}^{n_e\gamma} + n_1^{n_e\gamma}\hat{S}_{22}^{n_e\gamma} \tag{44}$$

4.2 Derivatives of BEM Formulations for Plates with Respect to Plate Thickness h

In this section, the BEM formulations for plates with respect to plate thickness h are presented.

4.2.1 Boundary Integral Equations

The derivatives of the Boundary integral equations seen in section 4.1 with respect to plate thickness h are presented here.

The derivative of the discretised BEM boundary integral equation for the plate membrane (equation (8)) with respect to plate thickness h is:

$$\begin{aligned}&C_{\alpha\beta,h}^{m}(\mathbf{x}^{n_c})u_\beta(\mathbf{x}^{n_c}) + C_{\alpha\beta}^{m}(\mathbf{x}^{n_c})u_{\beta,h}(\mathbf{x}^{n_c}) \\ &+ \sum_{n_e=1}^{N_e}\sum_{\gamma=1}^{M}P_{\alpha\beta,h}^{m,n_e\gamma}(\mathbf{x}^{n_c})u_\beta^{n_e\gamma} + \sum_{n_e=1}^{N_e}\sum_{\gamma=1}^{M}P_{\alpha\beta}^{m,n_e\gamma}(\mathbf{x}^{n_c})u_{\beta,h}^{n_e\gamma} \\ &= \sum_{n_e=1}^{N_e}\sum_{\gamma=1}^{M}Q_{\alpha\beta,h}^{m,n_e\gamma}(\mathbf{x}^{n_c})t_\beta^{n_e\gamma} + \sum_{n_e=1}^{N_e}\sum_{\gamma=1}^{M}Q_{\alpha\beta}^{m,n_e\gamma}(\mathbf{x}^{n_c})t_{\beta,h}^{n_e\gamma}\end{aligned} \tag{45}$$

where:

$$P_{\alpha\beta,h}^{m,n_e\gamma}(\mathbf{x}^{n_c}) = \fint_{-1}^{+1} T_{\alpha\beta,h}^{m}(\mathbf{x}^{n_c},\mathbf{x}(\eta))N^{n_e\gamma}(\eta)J^{n_e}(\eta)d\eta \tag{46}$$

$$Q_{\alpha\beta,h}^{m,n_e\gamma}(\mathbf{x}^{n_c}) = \int_{-1}^{+1} U_{\alpha\beta,h}^{m}(\mathbf{x}^{n_c},\mathbf{x}(\eta))N^{n_e\gamma}(\eta)J^{n_e}(\eta)d\eta \tag{47}$$

where $\mathbf{x}^{n_c}$, $n_c = 1, 2, \ldots, N_c$ (where $N_c = N_n$) is the collocation node, N_n is the number of nodes, N_e is the number of elements, and M is the number of nodes per element. $M = 3$ in the case of quadratic elements.

The derivative of the discretised BEM boundary integral equation for bending (equation (11)) with respect to plate thickness h is:

$$\begin{aligned} & C^b_{ij,h}(\mathbf{x}^{n_c}) w_j(\mathbf{x}^{n_c}) + C^b_{ij}(\mathbf{x}^{n_c}) w_{j,h}(\mathbf{x}^{n_c}) \\ & + \sum_{n_e=1}^{N_e} \sum_{\gamma=1}^{M} P^{b,n_e\gamma}_{ij,h}(\mathbf{x}^{n_c}) w^{n_e\gamma}_j + \sum_{n_e=1}^{N_e} \sum_{\gamma=1}^{M} P^{b,n_e\gamma}_{ij}(\mathbf{x}^{n_c}) w^{n_e\gamma}_{j,h} \\ & = \sum_{n_e=1}^{N_e} \sum_{\gamma=1}^{M} Q^{b,n_e\gamma}_{ij,h}(\mathbf{x}^{n_c}) p^{n_e\gamma}_j + \sum_{n_e=1}^{N_e} \sum_{\gamma=1}^{M} Q^{b,n_e\gamma}_{ij}(\mathbf{x}^{n_c}) p^{n_e\gamma}_{j,h} \\ & + q_3 \sum_{n_e=1}^{N_e} O^{b,n_e}_{i,h}(\mathbf{x}^{n_c}) \end{aligned} \tag{48}$$

where:

$$P^{b,n_e\gamma}_{ij,h}(\mathbf{x}^{n_c}) = \fint_{-1}^{+1} T^b_{ij,h}(\mathbf{x}^{n_c}, \mathbf{x}(\eta)) N^{n_e\gamma}(\eta) J^{n_e}(\eta) d\eta \tag{49}$$

$$Q^{b,n_e\gamma}_{ij,h}(\mathbf{x}^{n_c}) = \int_{-1}^{+1} U^b_{ij,h}(\mathbf{x}^{n_c}, \mathbf{x}(\eta)) N^{n_e\gamma}(\eta) J^{n_e}(\eta) d\eta \tag{50}$$

$$O^{b,n_e}_{i,h}(\mathbf{x}^{n_c}) = \int_{-1}^{+1} B^b_{i,h}(\mathbf{x}^{n_c}, \mathbf{x}(\eta)) J^{n_e}(\eta) d\eta \tag{51}$$

where:

$$\begin{aligned} B^b_{i,h}(\mathbf{x}^{n_c}, \mathbf{x}(\eta)) = & V^b_{i,\alpha h}(\mathbf{x}^{n_c}, \mathbf{x}(\eta)) n_\alpha(\mathbf{x}(\eta)) \\ & - \frac{\nu}{(1-\nu)\lambda^2} U^b_{i\alpha,h}(\mathbf{x}^{n_c}, \mathbf{x}(\eta)) n_\alpha(\mathbf{x}(\eta)) \\ & + \frac{2\nu\lambda_{,h}}{(1-\nu)\lambda^3} U^b_{i\alpha}(\mathbf{x}^{n_c}, \mathbf{x}(\eta)) n_\alpha(\mathbf{x}(\eta)) \end{aligned} \tag{52}$$

In the above equations, $T^b_{ij,h}$, $U^b_{ij,h}$, and $V^b_{i,\alpha h}$ are the derivatives of the fundamental solutions for plate bending, while $T_{\alpha\beta,h}$ and $U_{\alpha\beta,h}$ are the derivatives of the fundamental solutions for the membrane. The expressions for these fundamental solutions have been derived for the first time in this work and can be found in the Appendix. The terms $C^m_{\alpha\beta,h}$ and $C^b_{ij,h}$ are the derivatives of the free terms seen in equations (8) and (11) respectively and their values can be directly evaluated from a consideration of rigid body motion.

In BEM-based IDM the system of equations is $\mathbf{H}_{,h}\mathbf{u} + \mathbf{H}\mathbf{u}_{,h} = \mathbf{G}_{,h}\mathbf{t} + \mathbf{G}\mathbf{t}_{,h}$, where $\mathbf{H}$, $\mathbf{G}$, $\mathbf{u}$, and $\mathbf{t}$ are the same as defined in section 4.1, and $\mathbf{H}_{,h}$, $\mathbf{G}_{,h}$, $\mathbf{u}_{,h}$, and $\mathbf{t}_{,h}$ are their derivatives. This system of equations can be rewritten as:

$$\mathbf{A}\mathbf{X}_{,h} = \left[\mathbf{F}_{,h} - \mathbf{A}_{,h}\mathbf{X}\right] \tag{53}$$

where $\mathbf{A}$ and $\mathbf{X}$ can be obtained from equation (16). Since the right-hand side of equation (53) is known, LU decomposition can be used to obtain the unknown derivatives of boundary displacements and tractions $\mathbf{X}_{,h}$.

4.2.2 Displacements and Rotations at Internal Points

The derivatives of the displacements and rotations at internal points seen in section 4.1.2 with respect to plate thickness h are presented here.

The derivatives of the in-plane displacements at some internal point $\mathbf{X}^{n_i}$, $n_i = 1,2,\ldots,N_i$ (where N_i is the number of internal points) are:

$$\begin{aligned} & u_{\beta,h}(\mathbf{X}^{n_i}) \\ & + \sum_{n_e=1}^{N_e}\sum_{\gamma=1}^{M} P^{m,n_e\gamma}_{\alpha\beta,h}(\mathbf{X}^{n_i})u^{n_e\gamma}_{\beta} + \sum_{n_e=1}^{N_e}\sum_{\gamma=1}^{M} P^{m,n_e\gamma}_{\alpha\beta}(\mathbf{X}^{n_i})u^{n_e\gamma}_{\beta,h} \\ & = \sum_{n_e=1}^{N_e}\sum_{\gamma=1}^{M} Q^{m,n_e\gamma}_{\alpha\beta,h}(\mathbf{X}^{n_i})t^{n_e\gamma}_{\beta} + \sum_{n_e=1}^{N_e}\sum_{\gamma=1}^{M} Q^{m,n_e\gamma}_{\alpha\beta}(\mathbf{X}^{n_i})t^{n_e\gamma}_{\beta,h} \end{aligned} \tag{54}$$

where:

$$P^{m,n_e\gamma}_{\alpha\beta,h}(\mathbf{X}^{n_i}) = \int_{-1}^{+1} T^{m}_{\alpha\beta,h}(\mathbf{X}^{n_i},\mathbf{x}(\eta))N^{n_e\gamma}(\eta)J^{n_e}(\eta)d\eta \tag{55}$$

$$Q^{m,n_e\gamma}_{\alpha\beta,h}(\mathbf{X}^{n_i}) = \int_{-1}^{+1} U^{m}_{\alpha\beta,h}(\mathbf{X}^{n_i},\mathbf{x}(\eta))N^{n_e\gamma}(\eta)J^{n_e}(\eta)d\eta \tag{56}$$

The derivatives of the rotations w_1 and w_2, and vertical displacement (out-of-plane displacement) w_3, with respect to plate thickness h are:

$$\begin{aligned} & w_{j,h}(\mathbf{X}^{n_i}) \\ & + \sum_{n_e=1}^{N_e}\sum_{\gamma=1}^{M} P^{b,n_e\gamma}_{ij,h}(\mathbf{X}^{n_i})w^{n_e\gamma}_{j} + \sum_{n_e=1}^{N_e}\sum_{\gamma=1}^{M} P^{b,n_e\gamma}_{ij}(\mathbf{X}^{n_i})w^{n_e\gamma}_{j,h} \\ & = \sum_{n_e=1}^{N_e}\sum_{\gamma=1}^{M} Q^{b,n_e\gamma}_{ij,h}(\mathbf{X}^{n_i})p^{n_e\gamma}_{j} + \sum_{n_e=1}^{N_e}\sum_{\gamma=1}^{M} Q^{b,n_e\gamma}_{ij}(\mathbf{X}^{n_i})p^{n_e\gamma}_{j,h} \\ & + q_3\sum_{n_e=1}^{N_e} O^{b,n_e}_{i,h}(\mathbf{X}^{n_i}) \end{aligned} \tag{57}$$

where:

$$P^{b,n_e\gamma}_{ij,h}(\mathbf{X}^{n_i}) = \int_{-1}^{+1} T^{b}_{ij,h}(\mathbf{X}^{n_i},\mathbf{x}(\eta))N^{n_e\gamma}(\eta)J^{n_e}(\eta)d\eta \tag{58}$$

$$Q^{b,n_e\gamma}_{ij,h}(\mathbf{X}^{n_i}) = \int_{-1}^{+1} U^{b}_{ij,h}(\mathbf{X}^{n_i},\mathbf{x}(\eta))N^{n_e\gamma}(\eta)J^{n_e}(\eta)d\eta \tag{59}$$

$$O^{b,n_e}_{i,h}(\mathbf{X}^{n_i}) = \int_{-1}^{+1} B^{b}_{i,h}(\mathbf{X}^{n_i},\mathbf{x}(\eta))J^{n_e}(\eta)d\eta \tag{60}$$

and:

$$\begin{aligned} B^{b}_{i,h}(\mathbf{X}^{n_i},\mathbf{x}(\eta)) = {} & V^{b}_{i,\alpha h}(\mathbf{X}^{n_i},\mathbf{x}(\eta))n_\alpha(\mathbf{x}(\eta)) \\ & - \frac{\nu}{(1-\nu)\lambda^2}U^{b}_{i\alpha,h}(\mathbf{X}^{n_i},\mathbf{x}(\eta))n_\alpha(\mathbf{x}(\eta)) \\ & + \frac{2\nu\lambda_{,h}}{(1-\nu)\lambda^3}U^{b}_{i\alpha}(\mathbf{X}^{n_i},\mathbf{x}(\eta))n_\alpha(\mathbf{x}(\eta)) \end{aligned} \tag{61}$$

4.2.3 Boundary Stress Resultants

The derivative of the through thickness stress in a plate (equation (25)) with respect to plate thickness is:

$$\begin{aligned}\sigma_{\alpha\beta,h} =& -\frac{1}{h^2}N_{\alpha\beta}+\frac{1}{h}N_{\alpha\beta,h}\\ &+\frac{12(hx_{3,h}-3x_3)}{h^4}M_{\alpha\beta}+\frac{12x_3}{h^3}M_{\alpha\beta,h}\\ =& -\frac{1}{h^2}N_{\alpha\beta}+\frac{1}{h}N_{\alpha\beta,h}-\frac{24x_3}{h^4}M_{\alpha\beta}+\frac{12x_3}{h^3}M_{\alpha\beta,h}\end{aligned} \tag{62}$$

where $N_{\alpha\beta,h}$ is the derivative of the membrane stress resultants, $M_{\alpha\beta,h}$ is the derivative of the bending stress resultants, and $x_{3,h}$ is the derivative of x_3 where $-h/2 \leq x_3 \leq +h/2$ (see Figure 1). As mentioned in section 4.1, x_3 can be described in terms of a non-dimensional variable $\bar{x}_3$, such that $x_3 = \bar{x}_3 h$, where $-1/2 \leq \bar{x}_3 \leq +1/2$. Therefore, $x_{3,h} = \bar{x}_3$.

The derivative of the normal component of the local stress is:

$$\hat{N}^{n_e\gamma}_{1\alpha,h} = \hat{t}^{n_e\gamma}_{\alpha,h} \tag{63}$$

The derivative of the tangential component of the local stress is:

$$\hat{N}^{n_e\gamma}_{22,h} = \frac{1}{1-\nu}\left[\frac{E}{1+\nu}\hat{\varepsilon}^{n_e\gamma}_{22}+\frac{Eh}{1+\nu}\hat{\varepsilon}^{n_e\gamma}_{22,h}+\nu\hat{t}^{n_e\gamma}_{1,h}\right] \tag{64}$$

where $\hat{\varepsilon}^{n_e\gamma}_{22,h}$ is given by:

$$\hat{\varepsilon}^{n_e\gamma}_{22,h} = \frac{\hat{e}^{n_e\gamma}_{2\alpha}}{J^{n_e}(\eta_\gamma)}\sum_{\rho=1}^{M}\left(u^{n_e\rho}_{\alpha,h}\left(\frac{dN^{n_e\rho}(\eta)}{d\eta}\right)_{\eta=\eta_\gamma}\right) \tag{65}$$

The derivatives of the global membrane stresses $N^{n_e\gamma}_{\alpha\beta,h}$ can be calculated via:

$$N^{n_e\gamma}_{\alpha\beta,h} = \hat{e}_{\rho\alpha}\hat{e}_{\phi\beta}\hat{N}^{n_e\gamma}_{\rho\phi,h} \tag{66}$$

The derivatives of the global membrane stress resultants are:

$$\begin{aligned}N^{n_e\gamma}_{11,h} &= (n^{n_e\gamma}_1)^2\hat{N}^{n_e\gamma}_{11,h}+(n^{n_e\gamma}_2)^2\hat{N}^{n_e\gamma}_{22,h}-2n^{n_e\gamma}_1 n^{n_e\gamma}_2\hat{N}^{n_e\gamma}_{12,h}\\ N^{n_e\gamma}_{12,h} &= n^{n_e\gamma}_1 n^{n_e\gamma}_2(\hat{N}^{n_e\gamma}_{11,h}-\hat{N}^{n_e\gamma}_{22,h})\\ &\quad+\left[(n^{n_e\gamma}_1)^2-(n^{n_e\gamma}_2)^2\right]\hat{N}^{n_e\gamma}_{12,h}\\ N^{n_e\gamma}_{22,h} &= (n^{n_e\gamma}_2)^2\hat{N}^{n_e\gamma}_{11,h}+(n^{n_e\gamma}_1)^2\hat{N}^{n_e\gamma}_{22,h}+2n^{n_e\gamma}_1 n^{n_e\gamma}_2\hat{N}^{n_e\gamma}_{12,h}\end{aligned} \tag{67}$$

The derivatives of the out-of-plane stress resultants can be calculated in a similar manner as the in-plane stress resultants.

The derivative of the normal components of the tractions at node γ of element n_e are:

$$\hat{p}^{n_e\gamma}_{1,h} = n^{n_e\gamma}_1 p^{n_e\gamma}_{1,h}+n^{n_e\gamma}_2 p^{n_e\gamma}_{2,h} \tag{68}$$

The derivative of the tangential component of tractions is:

$$\hat{p}^{n_e\gamma}_{2,h} = -n^{n_e\gamma}_2 p^{n_e\gamma}_{1,h}+n^{n_e\gamma}_1 p^{n_e\gamma}_{2,h} \tag{69}$$

The derivative of the tangential component of the rotations is:

$$\hat{w}_{2,h}^{n_e\gamma} = -n_2^{n_e\gamma} w_{1,h}^{n_e\gamma} + n_1^{n_e\gamma} w_{2,h}^{n_e\gamma} \tag{70}$$

The local tangential strain is:

$$\hat{\chi}_{22,h}^{n_e\gamma} = \frac{\hat{e}_{2\alpha}^{n_e\gamma}}{J^{n_e}(\eta_\gamma)} \sum_{\rho=1}^{M} \left(w_{\alpha,h}^{n_e\rho} \left(\frac{dN^{n_e\rho}(\eta)}{d\eta} \right)_{\eta=\eta_\gamma} \right) \tag{71}$$

The derivatives of the local moments and shear stresses are:

$$\hat{M}_{11,h}^{n_e\gamma} = \hat{p}_{1,h}^{n_e\gamma} \tag{72}$$

$$\hat{M}_{12,h}^{n_e\gamma} = \hat{p}_{2,h}^{n_e\gamma} \tag{73}$$

$$\begin{aligned} \hat{M}_{22,h}^{n_e\gamma} =& \nu \hat{M}_{11,h}^{n_e\gamma} + D_{,h}(1-\nu^2)\hat{\chi}_{22}^{n_e\gamma} \\ &+ D(1-\nu^2)\hat{\chi}_{22,h}^{n_e\gamma} - \frac{2\lambda_{,h} q_3 \nu}{\lambda^3} \end{aligned} \tag{74}$$

$$\hat{S}_{11,h}^{n_e\gamma} = p_{3,h}^{n_e\gamma} \tag{75}$$

$$\begin{aligned} \hat{S}_{22,h}^{n_e\gamma} =& \frac{(1-\nu)(D_{,h}\lambda^2 + 2D\lambda_{,h}\lambda)}{2} \left[\hat{w}_2^{n_e\gamma} \right. \\ &\left. + \frac{1}{J^{n_e}(\eta_\gamma)} \sum_{\rho=1}^{M} \left(w_3^{n_e\rho} \left(\frac{dN^{n_e\rho}(\eta)}{d\eta} \right)_{\eta=\eta_\gamma} \right) \right] \\ &+ \frac{D(1-\nu)\lambda^2}{2} \left[\hat{w}_{2,h}^{n_e\gamma} \right. \\ &\left. + \frac{1}{J^{n_e}(\eta_\gamma)} \sum_{\rho=1}^{M} \left(w_{3,h}^{n_e\rho} \left(\frac{dN^{n_e\rho}(\eta)}{d\eta} \right)_{\eta=\eta_\gamma} \right) \right] \end{aligned} \tag{76}$$

The global moment stress resultants for node γ of element n_e are:

$$\begin{aligned} M_{11,h}^{n_e\gamma} &= (n_1^{n_e\gamma})^2 \hat{M}_{11,h}^{n_e\gamma} + (n_2^{n_e\gamma})^2 \hat{M}_{22,h}^{n_e\gamma} - 2n_1^{n_e\gamma} n_2^{n_e\gamma} \hat{M}_{12,h}^{n_e\gamma} \\ M_{12,h}^{n_e\gamma} &= n_1^{n_e\gamma} n_2^{n_e\gamma} (\hat{M}_{11,h}^{n_e\gamma} - \hat{M}_{22,h}^{n_e\gamma}) \\ &\quad + \left[(n_1^{n_e\gamma})^2 - (n_2^{n_e\gamma})^2 \right] \hat{M}_{12,h}^{n_e\gamma} \\ M_{22,h}^{n_e\gamma} &= (n_2^{n_e\gamma})^2 \hat{M}_{11,h}^{n_e\gamma} + (n_1^{n_e\gamma})^2 \hat{M}_{22,h}^{n_e\gamma} + 2n_1^{n_e\gamma} n_2^{n_e\gamma} \hat{M}_{12,h}^{n_e\gamma} \end{aligned} \tag{77}$$

The global shear stress resultants for node γ of element n_e are:

$$S_{1,h}^{n_e\gamma} = n_1^{n_e\gamma} \hat{S}_{11,h}^{n_e\gamma} - n_2^{n_e\gamma} \hat{S}_{22,h}^{n_e\gamma} \tag{78}$$

$$S_{2,h}^{n_e\gamma} = n_2^{n_e\gamma} \hat{S}_{11,h}^{n_e\gamma} + n_1^{n_e\gamma} \hat{S}_{22,h}^{n_e\gamma} \tag{79}$$

4.3 Validation

To validate the derived BEM formulations, results were compared with an analytical solution for a square simply supported plate subjected to uniform constant pressure presented in [36]. The square plate has edges of length a and thickness h, it is subjected to a uniform pressure q_3. All four edges of the plate are simply supported such that $w_3 = 0$ along the edges. The plate can be seen in Figure 5, and details of the plate are shown in Table 1.

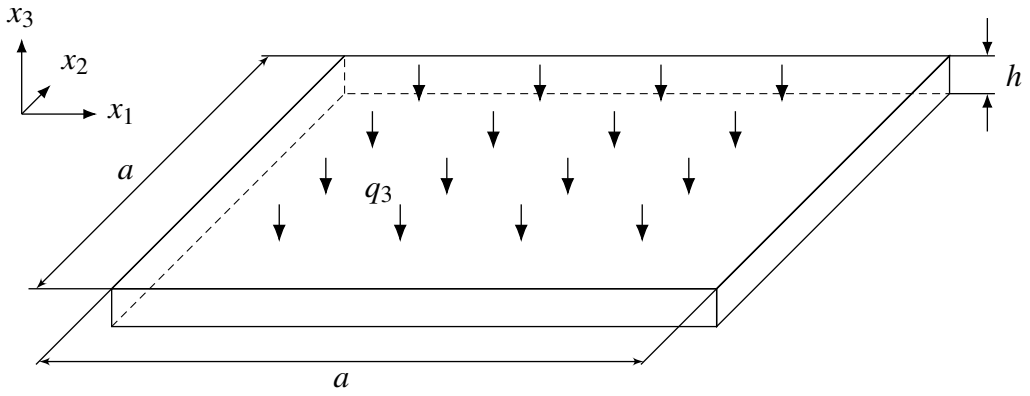

Figure 5: A square plate with edge length a and thickness h subjected to uniform constant pressure q_3. All four edges are simply supported such that $w_3 = 0$ along the edges.

Table 1: Properties of the plate used for validation.

Property	Description	Value
a	Plate edge length	1
h	Plate thickness	Variable
E	Young's modulus	1
ν	Poisson's ratio	0.3
q_3	Uniform pressure	1

The maximum vertical deflection w_3^{max} will occur in the centre of the plate. The solution given in [36] for the square plate is:

$$w_3^{max} = 0.00406 \frac{q_3 a^4}{D} \tag{80}$$

where D is the flexural stiffness:

$$D = \frac{Eh^3}{12(1-\nu^2)} \tag{81}$$

The derivative of equation (80) with respect to the thickness h is:

$$w_{3,h}^{max} = -0.00406 \frac{q_3 a^4 D_{,h}}{D^2} \tag{82}$$

where $D_{,h} = 3D/h$. Equation (82) is the exact solution for $w_{max,h}$.

The derivative $w_{3,h}^{max}$ was also calculated via IDM and the FDM for a range of stepsizes, and at different values for h. The percentage differences between the exact solution for $w_{3,h}^{max}$ and the values of

Table 2: Percentage differences (%) between the IDM and the exact solution, and percentage differences between the FDM and the exact solution, when calculating $w_{,h}^{max}$. The stepsize used with the FDM is shown in brackets.

h/a	FDM(1E-1)	FDM(1E-2)	FDM(1E-3)	FDM(1E-4)	FDM(1E-5)	IDM
1/10	30.90	9.65	7.66	7.46	7.45	7.44
1/20	25.78	5.57	3.68	3.49	3.47	3.47
1/30	24.28	4.37	2.50	2.31	2.30	2.29
1/40	23.56	3.78	1.93	1.74	1.73	1.73
1/50	23.13	3.43	1.59	1.41	1.39	1.39
1/100	22.30	2.77	0.94	0.76	0.74	0.74

$w_{3,h}^{max}$ obtained from the IDM and the FDM can be seen in Table 2. For both the FDM and the IDM, a BEM model was created of the square plate consisting of 32 quadratic elements. It can be seen that the stepsize used with the FDM has a significant impact on the difference between the FDM and the exact solution for $w_{3,h}^{max}$. Higher stepsizes cause greater instability, while lower stepsizes provide greater accuracy. The IDM results are in excellent agreement with the analytical solution.

In conclusion, the IDM has been successfully validated against an exact solution, and against the FDM. The IDM was shown to be more accurate than the FDM for most of the stepsizes tested. Furthermore, unlike the FDM, its accuracy was not dependent on the value of stepsizes, indicating the IDM is more robust and stable than the FDM.

5 Numerical Example

Section 4.3 demonstrated the high accuracy and robustness of the newly developed IDM. To now demonstrate its efficiency, the IDM is employed as part of a numerical example featuring the plate structure seen in Figure 6. In this numerical example, the geometrical design of this plate will be optimised in terms of its manufacturing cost and its reliability. The optimisation procedures used in this numerical example require the calculation of constraint derivatives, which can be calculated using either the IDM or the FDM. To determine the efficiency of the IDM, a comparison is made between the time required by IDM and the FDM to complete the optimisation at the end of this numerical example.

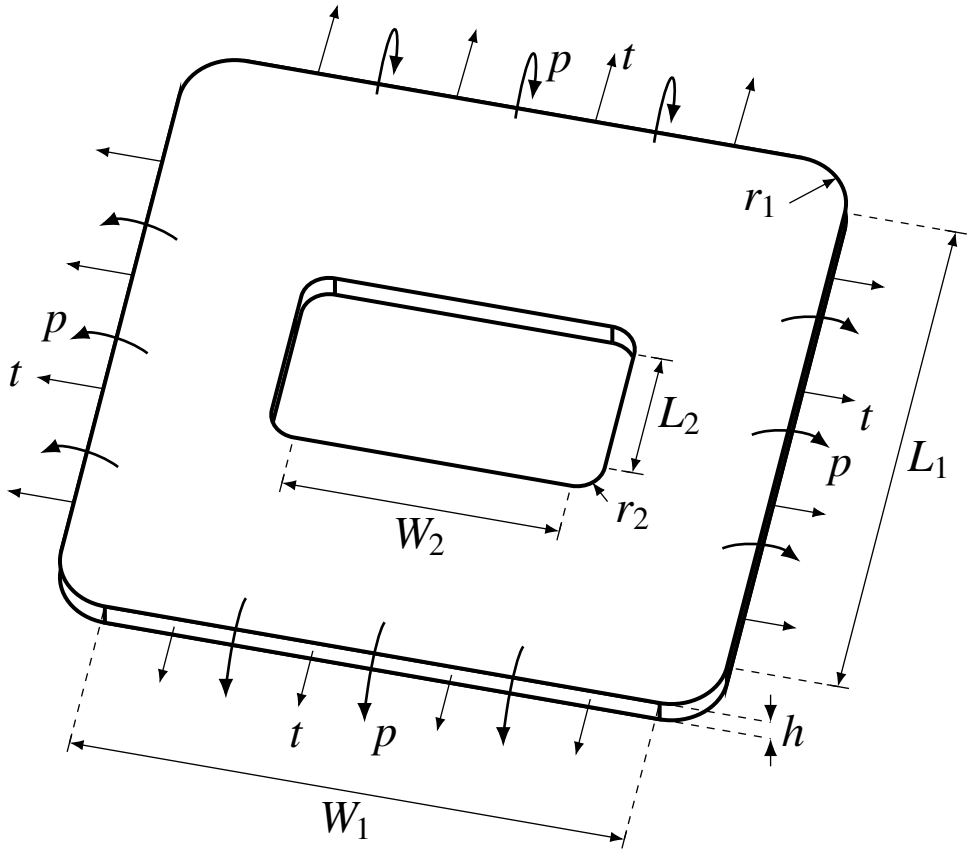

Figure 6: A plate structure subjected to tension and bending moments.

The plate is simply supported around its outer edge such that the vertical defelction of the plate is zero on its outer edge, and it is subjected to boundary tension and bending moments along this outer edge. It is composed of Aluminum 6061-T6, an aluminium alloy commonly found in aircraft structures due to its high strength and low weight. It has a Young's modulus E of 68.9 GPa, a Poisson's ratio of 0.33, and a tensile yield strength of 276 MPa. Material properties of Aluminum 6061-T6 can be found in [37]. The geometry of the plate is described by the geometrical variables: W_1, L_1, R_1, W_2, L_2, R_2, and h. These geometrical variables, along with the boundary tractions, boundary bending moments, and yield strength, are treated as random variables in the optimisation procedure. Details of the random variables can be seen in Table 3. A total of 112 quadratic elements were used in the BEM mesh of this plate structure.

Table 3: Details of the random variables, including their units, mean, and Coefficient of Variation (CoV).

Variable	Description	Units	Mean	CoV
W_1	Outer width	m	[0.8, 1.2]	0.01
L_1	Outer length	m	[0.8, 1.2]	0.01
R_1	Outer radius	m	[0.08, 0.12]	0.01
W_2	Inner width	m	[0.4, 0.6]	0.01
L_2	Inner length	m	[0.2, 0.3]	0.01
R_2	Inner radius	m	[0.04, 0.06]	0.01
h	Thickness	m	[0.04, 0.06]	0.01
t	Boundary traction	MN/m	0.9	0.10
p	Boundary moment	MN	0.01	0.10
σ_y	Tensile yield stress	MPa	276	0.10

The manufacturing cost of the plate is estimated using the approach outlined in section 2. To use this approach, a database was created that contains the details of 100 plates with a geometry similar to the plate shown in Figure 6. Details of this database can be seen in Table 4. By using this database with the approach outlined in section 2, the following formula for the manufacturing cost of the plate can be obtained:

$$\begin{aligned} Cost =& 278.51 + 59.42\ln(W_1) + 49.42\ln(L_1) \\ &+ 18.57\ln(R_1) - 12.04\ln(W_2) \\ &- 7.44\ln(L_2) + 64.43\ln(h) \end{aligned} \tag{83}$$

Table 4: Details of the database containing 100 plates with a geometry similar to the plate shown in Figure 6. The minimum, mean, and maximum values of each cost driver in the database are shown.

Variable	Minimum value	Mean value	Maximum value
W_1 (m)	0.85	1.00	1.15
L_1 (m)	0.85	0.99	1.15
R_1 (m)	0.085	0.099	0.115
W_2 (m)	0.425	0.493	0.574
L_2 (m)	0.213	0.252	0.287
R_2 (m)	0.0426	0.0494	0.0574
h (m)	0.0426	0.0507	0.0574
Manufacturing cost (€)	42.55	60.77	92.02

When run with the database, this formula demonstrated a high coefficient of determination of $R^2 = 0.82$ and $R_{adj} = 0.81$, indicating the high level of accuracy associated with this formula. By using this formula, the optimisation of the plate structure can now be conducted with respect to manufacturing cost.

To investigate the impact of optimising the plate with respect to reliability, two different approaches are investigated for the optimisation of the plate structure:

- Approach 1: Both the manufacturing cost and the reliability of the plate are considered during the optimisation procedure.

- Approach 2: Only the manufacturing cost of the plate is considered during the optimisation procedure.

Both approaches investigated in the following sections. It is expected that the optimal designs obtained from approaches 1 and 2 will be significantly different.

5.1 Manufacturing Cost Optimisation and RBDO

In this section, both the manufacturing cost and the reliability of the plate are considered during the optimisation procedure. In this case, the optimisation problem is:

$$\begin{aligned} &\text{Minimise} && Cost(\mathbf{d}) \\ &\text{Subject to} && g(\mathbf{Z}^*) \leq 0 \\ & && \mathbf{d}^L \leq \mathbf{d} \leq \mathbf{d}^U, \quad \mathbf{d} \in \mathbb{R}^{n_d} \end{aligned} \tag{84}$$

where $\mathbf{d} = [W_1, L_1, R_1, W_2, L_2, R_2, h]$ is the vector of design variables, and $n_d = 7$ is the number of design variables. The initial design of the plate is $\mathbf{d}_0 = [1, 1, 0.1, 0.5, 0.25, 0.05, 0.05]$. The lower and upper bounds of the design variables are: $\mathbf{d}^L = 0.8 \times \mathbf{d}_0$ and $\mathbf{d}^U = 1.2 \times \mathbf{d}_0$, respectively. The limit state function $g(\mathbf{Z})$ is:

$$g(\mathbf{Z}) = \sigma_{max}(\mathbf{Q}) - \sigma_y \tag{85}$$

where $\mathbf{Z} = [W_1, L_1, R_1, W_2, L_2, R_2, h, t, p, \sigma_y]$ is a vector of the random variables from Table 3 that influence g, and $\mathbf{Q} = [W_1, L_1, R_1, W_2, L_2, R_2, h, t, p]$ is a vector of the random variables from Table 3 that influence the maximum Von-Mises stress σ_{max} in the plate structure ($\mathbf{Q}$ is identical to $\mathbf{Z}$, except $\mathbf{Q}$ lacks σ_y).

The IDM, with the Performance Measure Approach (PMA) outlined in section 3.2, is used to solve the optimisation problem seen in equation (84). Similar to the previous section, the optimisation was conducted using Matlab© with the nonlinear multivariable optimisation routine 'fmincon'. The optimal plate designs from 'fmincon' for a range of target reliability indices β_{target} can be seen in Table 5, and diagrams of these optimal designs can be seen in Figure 7. It can be seen from Table 5 and Figure 7 that the plate becomes thicker and wider as β_{target} increases, which makes sense given that the maximum stress is expected to occur at the corners of the central hole. To verify that these optimal designs achieve the desired reliabilities, the reliability index from the FORM β_{FORM} was calculated for each of the optimal designs and are presented in Table 5. It can be seen that β_{FORM} and β_{target} are in very good agreement; the difference between them is less than 0.1%.

Table 5: Optimisation results from the IDM for a range of target reliability indices.

β_{target}	W_1 (m)	L_1 (m)	R_1 (m)	W_2 (m)	L_2 (m)	R_2 (m)	h (m)	$Cost$ (€)	β_{FORM}
2	0.800	0.800	0.0800	0.400	0.200	0.0600	0.0409	24.29	2.000
3	0.800	0.800	0.0800	0.400	0.200	0.0600	0.0455	31.24	3.000
4	0.800	0.800	0.0800	0.400	0.200	0.0600	0.0514	39.13	4.000
5	0.800	0.800	0.0800	0.400	0.200	0.0600	0.0594	48.37	5.000
6	0.910	1.141	0.1200	0.400	0.200	0.0600	0.0600	81.75	6.000

The target reliability indices β_{target} and the corresponding target probabilities of failure $P_{F,target}$ for each of the optimal designs can be seen in Figure 8. It can be seen that the probability of failure drops by a magnitude of 8 as the reliability index increases; the probability of failure corresponding

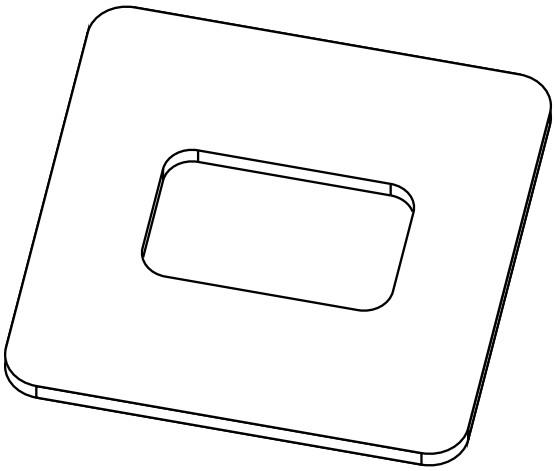

(a) $\beta_{target} = 2$

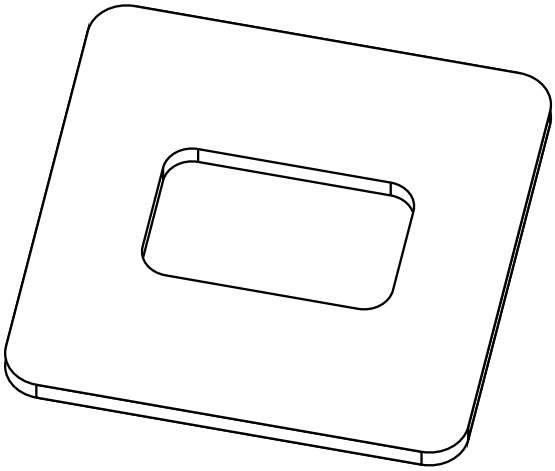

(b) $\beta_{target} = 3$

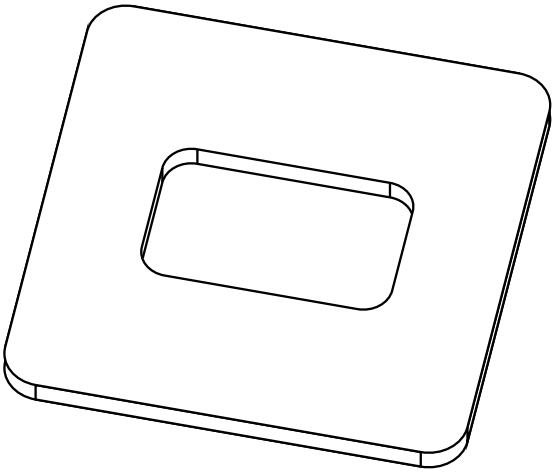

(c) $\beta_{target} = 4$

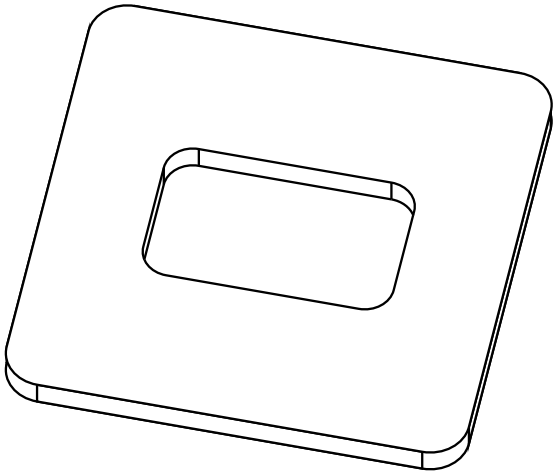

(d) $\beta_{target} = 5$

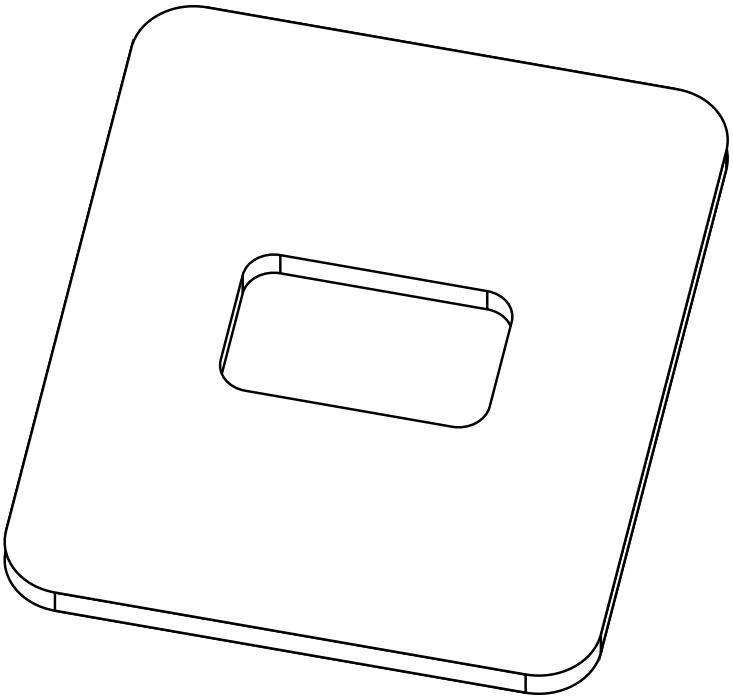

(e) $\beta_{target} = 6$

Figure 7: Optimal plate designs when both the manufacturing cost and the reliability of the plate are considered during the optimisation procedure. The optimal designs are a range of target reliability indices β_{target} is shown. The designs are to scale.

to a reliability index of 2 is 2.3%, while for a reliability index of 6 it is 9.9×10^{-8}%. The cost on the other hand, increases from 24.92 € for a reliability index of 2, to 81.75 € for a reliability index of 6, a percentage increase of 236%.

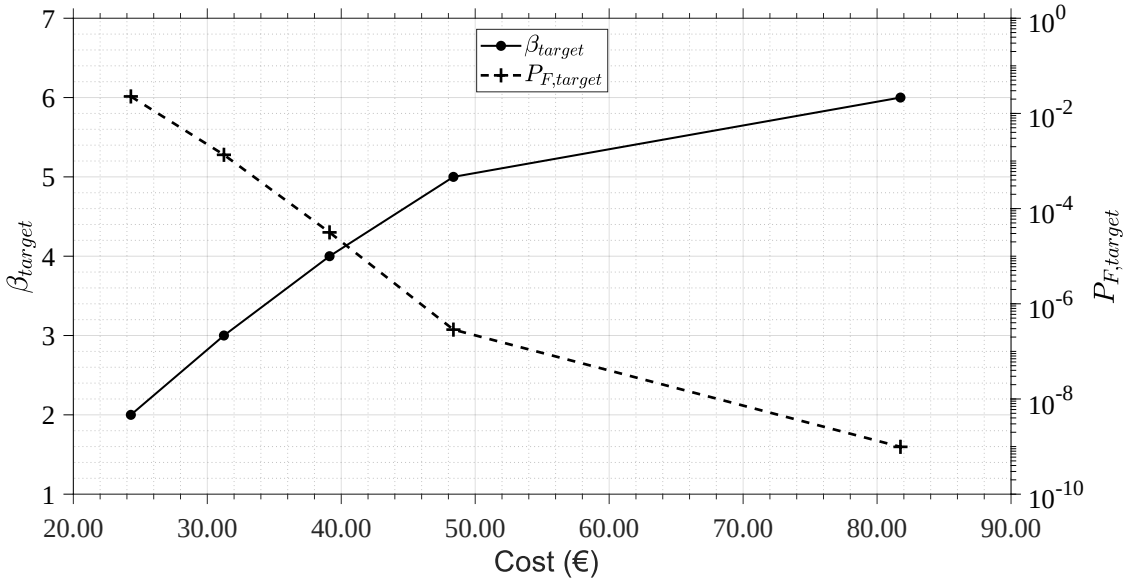

Figure 8: Target reliability indices β_{target} and the corresponding target probabilities of failure $P_{F,target}$ for each of the optimal designs.

The optimisation history from the IDM for a range of target reliability indices can be seen in Figure 9. It can be seen that the significantly more iterations were required to obtain convergence for the case with $\beta_{target} = 6$. This can partly be explained by the fact that the jump in the probability of failure between $\beta_{target} = 5$ to $\beta_{target} = 6$ was by a magnitude of 3, while previous jumps in the probability of failure were only by a magnitude of 2 or 1. Therefore, significantly more alterations were required to the geometry of the design, increasing the number of iterations needed.

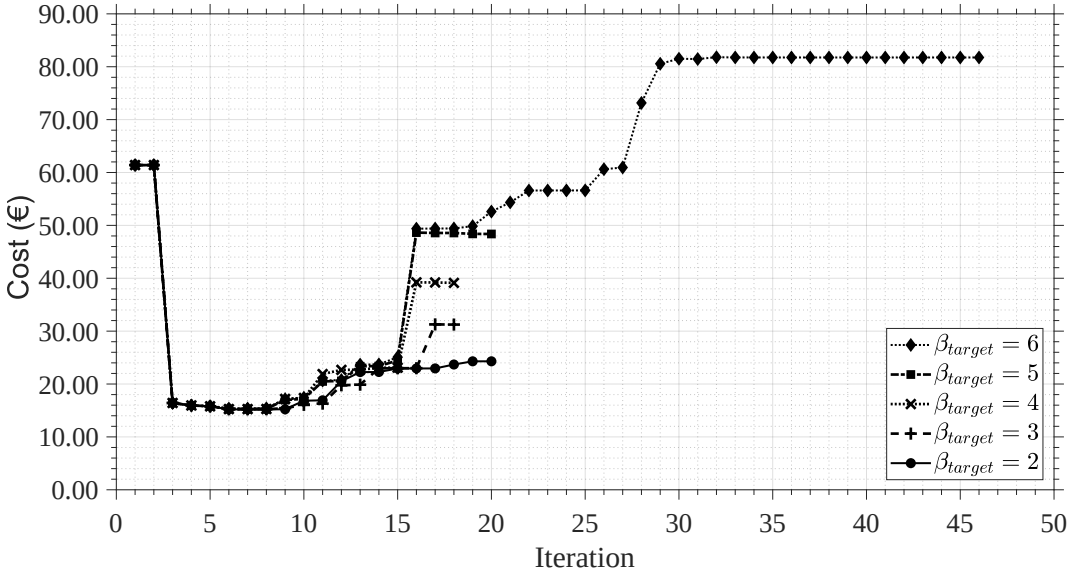

Figure 9: Optimisation history from the IDM for a range of target reliability indices β_{target}.

Up until this point, only the optimisation results with the IDM have been presented. This is because section 4.3 demonstrated the high accuracy and robustness of the IDM, and its excellent

agreement with the FDM when calculating the constraint derivatives required by the optimisation procedure. To demonstrate the efficiency of the IDM, the CPU time required by the IDM to optimise the plate structure was compared to the CPU time required by the FDM. The average CPU time required by the IDM and the FDM to complete one optimisation iteration was calculated by averaging over 100 optimisation iterations. The results are shown in Table 6. It was found that the IDM was, on average, 19% faster than the FDM. For a single iteration or for a simple structure, this increase in efficiency may not be significant, but it could be very useful for a more complex structure that requires many iterations. In this case, the IDM could significantly reduce the total optimisation time.

A flowchart for designing the optimisation code used in this section can be seen in Figure 10.

Table 6: Mean CPU time to complete one optimisation iteration when using the FDM or the IDM.

Method	$t_{iteration}$ (s)
FDM	98.72
IDM	79.78

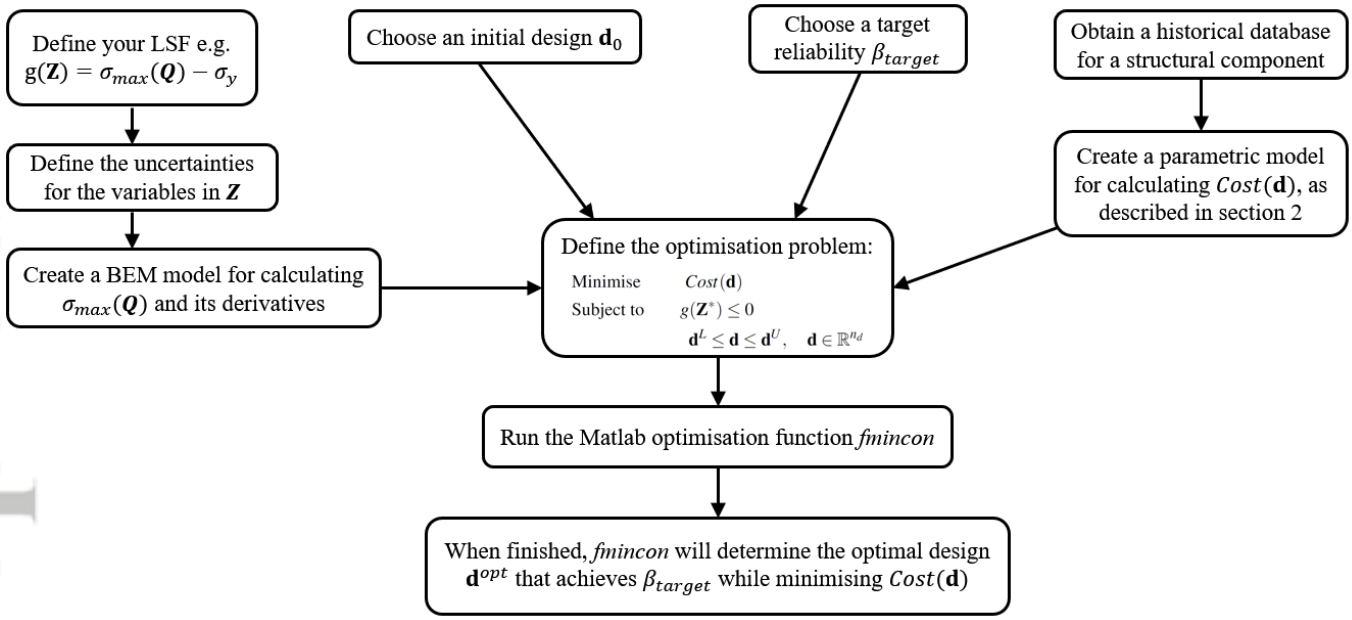

Figure 10: A flowchart for designing the optimisation code used in section 5.1.

5.2 Manufacturing Cost Optimisation

In this section, only the manufacturing cost of the plate is considered during the optimisation procedure. In this case, the optimisation problem is:

$$\begin{aligned} &\text{Minimise} && Cost(\mathbf{d}) \\ &\text{Subject to} && \mathbf{d}^L \leq \mathbf{d} \leq \mathbf{d}^U, \quad \mathbf{d} \in \mathbb{R}^{n_d} \end{aligned} \tag{86}$$

where $\mathbf{d} = [W_1, L_1, R_1, W_2, L_2, R_2, h]$ is the vector of design variables, and $n_d = 7$ is the number of design variables. The initial design of the plate $\mathbf{d}_0$, as well as the lower and upper bounds of the design variables, $\mathbf{d}^L$ and $\mathbf{d}^U$, are the same as in the previous section.

The optimisation problem in equation (86) was conducted using Matlab© with the nonlinear multivariable optimisation routine 'fmincon'. The optimal plate design from 'fmincon' can be seen in Table 7, and a diagram of this optimal design can be seen in Figure 11. It can be seen that the values of the design variables are equal to their lower or upper bounds, except for R_2 which stayed at its initial value since it is not included in the regression model seen in equation (83). The manufacturing cost was reduced from 61.40 € for the initial design, to only 15.06 € for the optimal design; this represents a significant reduction in cost. However, when evaluating the reliability of this design using the limit state function shown in equation (85), a probability of failure of $P_F = 99.6\%$ is obtained. This probability of failure is significantly higher than that the highest obtained from the previous section, which was only 2.3%. Such a high probability is unacceptable, and highlights the importance of taking into account both manufacturing costs and reliability when optimising the design of a structure.

A flowchart for designing the optimisation code used in this section can be seen in Figure 12.

Table 7: Optimal plate design when only the manufacturing cost of the plate is considered during the optimisation procedure.

W_1 (m)	L_1 (m)	R_1 (m)	W_2 (m)	L_2 (m)	R_2 (m)	h (m)	*Cost* (€)
0.800	0.800	0.0800	0.600	0.300	0.0500	0.0400	15.06

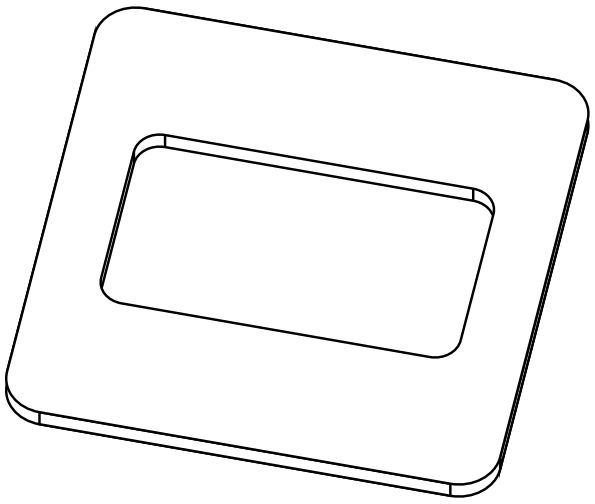

Figure 11: The optimal plate design when only the manufacturing cost of the plate is considered during the optimisation procedure.

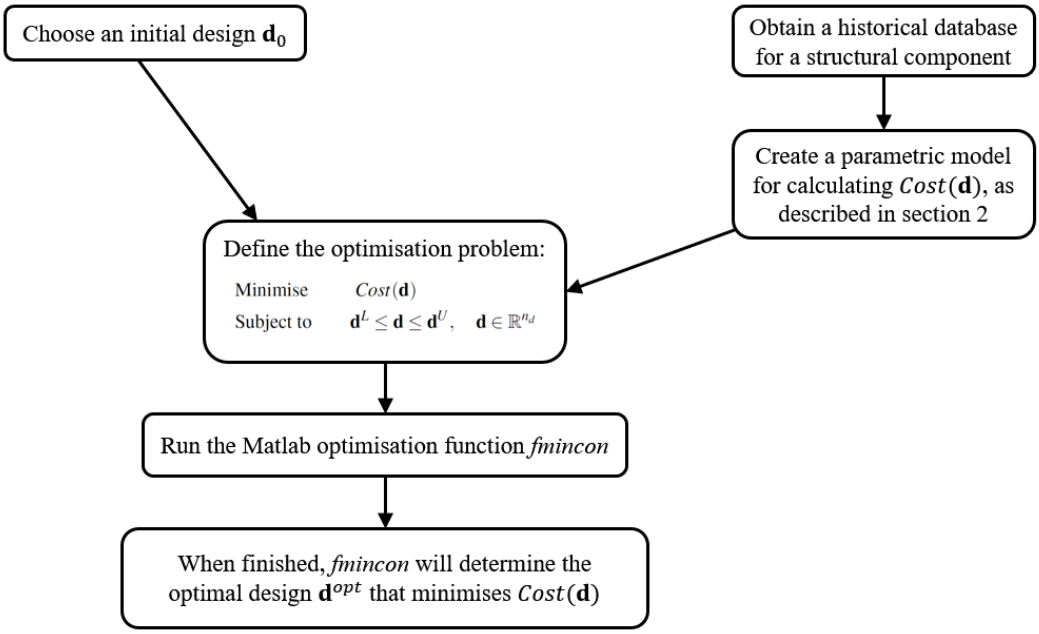

Figure 12: A flowchart for designing the optimisation code used in section 5.2.

6 Conclusions

In conclusion, this paper presented a novel methodology for the manufacturing cost and reliability-based optimisation of plate structures with the Boundary Element Method (BEM), with the aim of improving the accuracy, robustness, and efficiency of the optimisation of plate structures. The derivatives of the BEM plate formulations, with respect to plate thickness, were derived for the first time and used as part of an Implicit Differentiation Method (IDM), enabling the full shape optimisation of plate structures with the BEM. These implicit derivatives were validated against derivatives obtained from the Finite Difference Method (FDM) and from an analytical solution. The IDM was found to be in excellent agreement with the analytical solution, and more robust and accurate than the FDM for most of the step-sizes investigated. To demonstrate the efficiency of the newly developed IDM, it was employed as part of a numerical example involving the Reliability-Based Design Optimisation (RBDO) and manufacturing cost optimisation of a plate structure. The design parameters in the optimisation included all the geometric parameters describing the shape of the structure. Results indicate that the IDM is 19% faster, on average, in terms of CPU time than the FDM when performing this optimisation. Such results represent a significant reduction in the computation time associated with the optimisation of complex structures.

Acknowledgements

This project has received funding from the Clean Sky 2 Joint Undertaking (JU) under grant agreement No. 864154 Project MASCOT. The JU receives support from the European Union's Horizon 2020 research and innovation programme and the Clean Sky 2 JU members other than the Union.

Conflict of interest

The authors declare that they have no conflict of interest.

Data availability statement

The data that support the findings of this study are available from the corresponding author upon reasonable request.

Appendix A Formulations for the BEM-based IDM

The fundamental solutions for the membrane and for plate bending can be found in [32]. The derivatives of these fundamental solutions with respect to plate thickness h have been derived for the first time in this work and are presented in this Appendix.

A.1 Useful Definitions

The following relationships are used in the fundamental solutions derived in this work.

$$r_\alpha = x_\alpha - x'_\alpha \tag{87}$$

$$r = \sqrt{r_\alpha^2} = \sqrt{r_1^2 + r_2^2} \tag{88}$$

$$r_{,\alpha} = \frac{r_\alpha}{r} \tag{89}$$

$$\frac{\partial r}{\partial n} = r_{,n} = n_\alpha r_{,\alpha} = n_1 r_{,1} + n_2 r_{,2} \tag{90}$$

Derivatives with respect to direction x_α:

$$\frac{\partial f(r)}{\partial x_\alpha} = \frac{\partial f(r)}{\partial r}\frac{\partial r}{\partial x_\alpha} = \frac{\partial f(r)}{\partial r} r_{,\alpha} \tag{91}$$

$$r_{,\alpha\beta} = \frac{1}{r}\Big(\delta_{\alpha\beta} - r_{,\alpha} r_{,\beta}\Big) \tag{92}$$

$$(r_{,n})_{,\alpha} = \frac{1}{r}\Big(n_\alpha - r_{,\alpha} r_{,n}\Big) \tag{93}$$

Useful definitions for plate bending:

$$\lambda = \frac{\sqrt{10}}{h} \tag{94}$$

$$z = \lambda r \tag{95}$$

$$B = \frac{Eh}{1-\nu^2} \tag{96}$$

$$D = \frac{Eh^3}{12(1-\nu^2)} \tag{97}$$

$$C = \frac{D(1-\nu)\lambda^2}{2} \tag{98}$$

where λ is the shear factor, h is plate thickness, and B, D, and C represent the tension stiffness, bending stiffness, and shear stiffness of the plate respectively.

Their derivatives with respect to plate thickness h are:

$$\lambda_{,h} = -\frac{\sqrt{10}}{h^2} = -\frac{\lambda}{h} \tag{99}$$

$$z_{,h} = \lambda_{,h} r = -\frac{\lambda r}{h} = -\frac{z}{h} \tag{100}$$

$$B_{,h} = \frac{E}{1-\nu^2} = \frac{B}{h} \tag{101}$$

$$D_{,h} = \frac{3Eh^2}{12(1-\nu^2)} = \frac{3D}{h} \tag{102}$$

$$C_{,h} = \frac{(1-\nu)(D_{,h}\lambda^2 + 2D\lambda_{,h}\lambda)}{2} = \frac{D(1-\nu)\lambda^2}{2h} = \frac{C}{h} \tag{103}$$

We also have:

$$A(z) = K_0(z) + \frac{2}{z}\left[K_1(z) - \frac{1}{z}\right] \tag{104}$$

$$B(z) = K_0(z) + \frac{1}{z}\left[K_1(z) - \frac{1}{z}\right] \tag{105}$$

where $K_0(z)$ and $K_1(z)$ are modified Bessel functions of the second kind.

$$A_{,h}(z) = K_{0,h}(z) - \frac{2\lambda_{,h} r K_1(z)}{z^2} + \frac{2K_{1,h}(z)}{z} + \frac{4\lambda_{,h} r}{z^3} \tag{106}$$

$$B_{,h}(z) = K_{0,h}(z) - \frac{\lambda_{,h} r K_1(z)}{z^2} + \frac{K_{1,h}(z)}{z} + \frac{2\lambda_{,h} r}{z^3} \tag{107}$$

where $K_{0,h}(z)$ and $K_{1,h}(z)$ are:

$$K_{0,h}(z) = -\lambda_{,h} r K_1(z) \tag{108}$$

$$K_{1,h}(z) = -\lambda_{,h} r\left(K_0(z) + \frac{K_1(z)}{z}\right) \tag{109}$$

A.2 Membrane Fundamental Solution Derivatives

The derivatives of the membrane fundamental solutions with respect to plate thickness h are:

$$U_{\alpha\beta,h} = -\frac{1+\nu}{4\pi E h^2(1-\nu)}\left[r_{,\alpha} r_{,\beta} - (3-4\nu)\ln(r)\delta_{\alpha\beta}\right] \tag{110}$$

$$T_{\alpha\beta,h} = 0 \tag{111}$$

A.3 Plate Bending Fundamental Solution Derivatives

The derivatives of the plate bending fundamental solutions with respect to plate thickness h are:

For $U^b_{ij,h}$:

$$U^b_{\alpha\beta,h} = -\frac{D_{,h}}{8\pi D^2(1-\nu)}\left\{\left[8B(z) - (1-\nu)(2\ln z - 1)\right]\delta_{\alpha\beta} - \left[8A(z) + 2(1-\nu)\right] r_{,\alpha} r_{,\beta}\right\} \tag{112}$$
$$+\frac{1}{8\pi D(1-\nu)}\left\{\left[8B_{,h}(z) - 2(1-\nu)\frac{z_{,h}}{z}\right]\delta_{\alpha\beta} - \left[8A_{,h}(z) + 2(1-\nu)\right] r_{,\alpha} r_{,\beta}\right\}$$

$$U^b_{\alpha 3,h} = -\frac{D_{,h}}{8\pi D^2}\left(2\ln z - 1\right) r r_{,\alpha} + \frac{1}{4\pi D}\frac{z_{,h}}{z} r r_{,\alpha} \tag{113}$$

$$U^b_{3\alpha,h} = -U^b_{\alpha 3,h} \tag{114}$$

$$\begin{aligned} U^b_{33,h} = &-\frac{D_{,h}\lambda + 2\lambda_{,h}D}{8\pi(1-\nu)D^2\lambda^3}\left[(1-\nu)z^2(\ln z - 1) - 8\ln z\right] \\ &+ \frac{1}{8\pi(1-\nu)D\lambda^2}\left[(1-\nu)(2\ln z - 1)z_{,h}z - 8\frac{z_{,h}}{z}\right] \end{aligned} \tag{115}$$

For $T^b_{ij,h}$:

$$\begin{aligned} T^b_{\alpha\beta,h} = -\frac{1}{4\pi r}\Bigg[&2\Big(2A_{,h}(z) + z_{,h}K_1(z) + zK_{1,h}(z)\Big)\Big(\delta_{\alpha\beta}r_{,n} + r_{,\beta}n_\alpha\Big) + 4A_{,h}(z)r_{,\alpha}n_\beta \\ &- 4\Big(4A_{,h}(z) + z_{,h}K_1(z) + zK_{1,h}(z)\Big)r_{,\alpha}r_{,\beta}r_{,n}\Bigg] \end{aligned} \tag{116}$$

$$T^b_{\alpha 3,h} = \frac{2\lambda\lambda_{,h}}{2\pi}\Big[B(z)n_\alpha - A(z)r_{,\alpha}r_{,n}\Big] + \frac{\lambda^2}{2\pi}\Big[B_{,h}(z)n_\alpha - A_{,h}(z)r_{,\alpha}r_{,n}\Big]$$

$$T^b_{3\alpha,h} = -\frac{(1+\nu)}{4\pi}\frac{z_{,h}}{z}n_\alpha \tag{117}$$

$$T^b_{33,h} = 0 \tag{118}$$

For $V^b_{i,\beta h}$:

$$V^b_{\alpha,\beta h} = -\frac{D_{,h}r^2}{128\pi D^2}\Big[\left(4\ln z - 5\right)\delta_{\alpha\beta} + 2\left(4\ln z - 3\right)r_{,\alpha}r_{,\beta}\Big] + \frac{r^2}{32\pi D}\frac{z_{,h}}{z}\Big[\delta_{\alpha\beta} + 2r_{,\alpha}r_{,\beta}\Big] \tag{119}$$

$$\begin{aligned} V^b_{3,\beta h} = &\frac{D_{,h}\lambda + 2\lambda_{,h}D}{128\pi D^2(1-\nu)\lambda^3} r r_{,\beta}\left[32\left(2\ln z - 1\right) - z^2(1-\nu)(4\ln z - 5)\right] \\ &- \frac{1}{64\pi D(1-\nu)\lambda^2} r r_{,\beta}\left[32\frac{z_{,h}}{z} - z_{,h}z(1-\nu)(4\ln z - 3)\right] \end{aligned} \tag{120}$$

References

[1] A. Tafreshi. Shape optimization of two-dimensional anisotropic structures using the boundary element method. *The Journal of Strain Analysis for Engineering Design*, 38(3), 2003.

[2] K. Abe, S. Kazama, and K. Koro. A boundary element approach for topology optimization problem using the level set method. *Communications in Numerical Methods in Engineering*, 23(5):405–416, 2006.

[3] G. K. Sfantos and M. H. Aliabadi. A boundary element sensitivity formulation for contact problems using the implicit differentiation method. *Engineering Analysis with Boundary Elements*, 30(1):22–30, 2006.

[4] A. Canelas, J. Herskovits, and J. C. F. Telles. Shape optimization using the boundary element method and a sand interior point algorithm for constrained optimization. *Computers & Structures*, 86(13-14):1517–1526, 2008.

[5] B. Ullah and J. Trevelyan. Correlation between hole insertion criteria in a boundary element and level set based topology optimisation method. *Engineering Analysis with Boundary Elements*, 37(11):1457–1470, 2013.

[6] Y. Chang, H. Cheng, M. Chiu, and Y. Chien. Shape optimisation of multi-chamber acoustical plenums using bem, neural networks, and ga method. *Archives of Acoustics*, 41(1):43–53, 2016.

[7] B. Ullah and J. Trevelyan. A boundary element and level set based topology optimisation using sensitivity analysis. *Engineering Analysis with Boundary Elements*, 70:80–98, 2016.

[8] C. Liu, L. Chen, W. Zhao, and H. Chen. Shape optimization of sound barrier using an isogeometric fast multipole boundary element method in two dimensions. *Engineering Analysis with Boundary Elements*, 85:142–157, 2017.

[9] B. Ullah, J. Trevelyan, and I. Siraj ul. A boundary element and level set based bi-directional evolutionary structural optimisation with a volume constraint. *Engineering Analysis with Boundary Elements*, 80:152–161, 2017.

[10] T. Takahashi, T. Yamamoto, Y. Shimba, H. Isakari, and T. Matsumoto. A framework of shape optimisation based on the isogeometric boundary element method toward designing thin-silicon photovoltaic devices. *Engineering with Computers*, 35(2):423–449, 2018.

[11] K. Matsushima, H. Isakari, T. Takahashi, and T. Matsumoto. A topology optimisation of composite elastic metamaterial slabs based on the manipulation of far-field behaviours. *Structural and Multidisciplinary Optimization*, 63(1):231–243, 2020.

[12] P. Maduramuthu and R. T Fenner. Three-dimensional shape design optimization of holes and cavities using the boundary element method. *The Journal of Strain Analysis for Engineering Design*, 39(1), 2004.

[13] A. Brancati, M. H. Aliabadi, and V. Mallardo. A bem sensitivity formulation for three-dimensional active noise control. *International Journal for Numerical Methods in Engineering*, 90(9):1183–1206, 2012.

[14] K. Bandara, F. Cirak, G. Of, O. Steinbach, and J. Zapletal. Boundary element based multiresolution shape optimisation in electrostatics. *Journal of Computational Physics*, 297:584–598, 2015.

[15] B. Ullah, J. Trevelyan, and I. Ivrissimtzis. A three-dimensional implementation of the boundary element and level set based structural optimisation. *Engineering Analysis with Boundary Elements*, 58:176–194, 2015.

[16] L. L. Chen, H. Lian, Z. Liu, H. B. Chen, E. Atroshchenko, and S. P. A. Bordas. Structural shape optimization of three dimensional acoustic problems with isogeometric boundary element methods. *Computer Methods in Applied Mechanics and Engineering*, 355:926–951, 2019.

[17] S. Gaggero, G. Vernengo, D. Villa, and L. Bonfiglio. A reduced order approach for optimal design of efficient marine propellers. *Ships and Offshore Structures*, 15(2):200–214, 2019.

[18] S. Li, J. Trevelyan, Z. Wu, H. Lian, D. Wang, and W. Zhang. An adaptive svd–krylov reduced order model for surrogate based structural shape optimization through isogeometric boundary element method. *Computer Methods in Applied Mechanics and Engineering*, 349:312–338, 2019.

[19] N. G. Babouskos and J. T. Katsikadelis. Optimum design of thin plates via frequency optimization using bem. *Archive of Applied Mechanics*, 85(9-10):1175–1190, 2014.

[20] L. Morse, Z. Sharif Khodaei, and M. H. Aliabadi. A dual boundary element based implicit differentiation method for determining stress intensity factor sensitivities for plate bending problems. *Engineering Analysis with Boundary Elements*, 106:412–426, 2019.

[21] S. Mellings and M. H. Aliabadi. Dual boundary element formulation for inverse potential problems in crack identification. *Engineering Analysis with Boundary Elements*, 12(4), 1993.

[22] S. Mellings and M. H. Aliabadi. Flaw identification using the boundary element method. *International Journal for Numerical Methods in Engineering*, 38(3), 1995.

[23] V. Mallardo and M. H. Aliabadi. A bem sensitivity and shape identification analysis for acoustic scattering in fluid–solid problems. *International Journal for Numerical Methods in Engineering*, 41(8), 1998.

[24] C. Alessandri and V. Mallardo. Crack identification in two-dimensional unilateral contact mechanics with the boundary element method. *Computational Mechanics*, 24, 1999.

[25] V. Mallardo and C. Alessandri. Inverse problems in the presence of inclusions and unilateral constraints a boundary element approach. *Computational Mechanics*, 26, 2000.

[26] X. Huang and M. H. Aliabadi. Probabilistic fracture mechanics by the boundary element method. *International Journal of Fracture*, 171(1):51–64, 2011.

[27] X. Huang and M.H. Aliabadi. A boundary element method for structural reliability. volume 627 of *Key Engineering Materials*. Trans Tech Publications Ltd, 2015.

[28] L. Morse, Z. Sharif Khodaei, and M. H. Aliabadi. A multi-fidelity boundary element method for structural reliability analysis with higher-order sensitivities. *Engineering Analysis with Boundary Elements*, 104:183–196, 2019.

[29] S. Mellings and M. H. Aliabadi. Three-dimensional flaw identification using inverse analysis. *International Journal of Engineering Science*, 34(4), 1996.

[30] NASA. Nasa cost estimating handbook version 4.0 - appendix c: Cost estimating methodologies. Report, 2015.

[31] B. D. Youn, K. K. Choi, and Y. H. Park. Hybrid analysis method for reliability-based design optimization. *Journal of Mechanical Design*, 125(2):221–232, 2003.

[32] M. H. Aliabadi. *The Boundary Element Method: Applications in solids and structures*, volume 2. John Wiley and Sons, 2002.

[33] C. Di Pisa and M. H. Aliabadi. Boundary element analysis for multi-layered panels and structures. Report, Queen Mary University of London, 2005.

[34] T. Dirgantara and M. H. Aliabadi. Crack growth analysis of plates loaded by bending and tension using dual boundary element method. *International Journal of Fracture*, 105(1):27–47, 1999.

[35] J. C. F. Telles. A self adaptive coordinate transformation for efficient numerical evaluation of general boundary element integrals. *International Journal for Numerical Methods in Engineering*, 24(5):959–973, 1987.

[36] S. Timoshenko. *Theory of Plates and Shells*. McGraw Hill, New York, 1959.

[37] MatWeb. Aluminum 6061-T6. `http://www.matweb.com/search/datasheet_print.aspx?matguid=1b8c06d0ca7c456694c7777d9e10be5b`, 2021. [Online; accessed 25-May-2021].